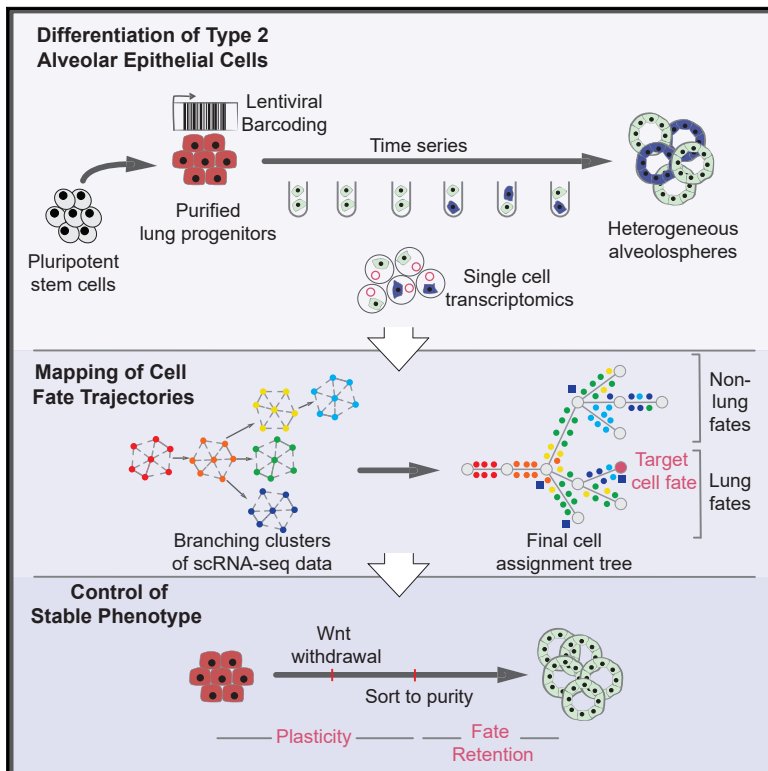


Cell Stem Cell

Reconstructed Single-Cell Fate Trajectories Define Lineage Plasticity Windows during Differentiation of Human PSC-Derived Distal Lung Progenitors

Graphical Abstract



Authors

Killian Hurley, Jun Ding, Carlos Villacorta-Martin, ..., Fernando Camargo, Ziv Bar-Joseph, Darrell N. Kotton

Correspondence

zivbj@andrew.cmu.edu (Z.B.-J.), dkotton@bu.edu (D.N.K.)

In Brief

Hurley et al. show that a combination of single-cell transcriptomics, computational modeling, and DNA barcoding can map cell-fate trajectories, predicting signaling pathways, transcription factors, and the time of activation for optimizing cell fate, as pluripotent stem cell-derived lung progenitors differentiate toward self-renewing lung alveolar epithelial cells.

Highlights

- Only a subset of PSC-lung progenitors maintain cell fate as they differentiate to iAEC2
- NKX2-1⁺ progenitor plasticity allows clonal divergence into alternative non-lung fates
- Continuous State Hidden Markov model predicts potential fate optimizing interventions
- Modulation of Wnt results in a stable iAEC2 phenotype with near limitless self-renewal

Reconstructed Single-Cell Fate Trajectories Define Lineage Plasticity Windows during Differentiation of Human PSC-Derived Distal Lung Progenitors

Killian Hurley,^{1,2,3,4,12} Jun Ding,^{5,12} Carlos Villacorta-Martin,¹ Michael J. Herriges,^{1,2} Anjali Jacob,^{1,2} Marall Vedaie,^{1,2} Konstantinos D. Alysandratos,^{1,2} Yuliang L. Sun,^{1,2} Chieh Lin,⁶ Rhiannon B. Werder,^{1,2} Jessie Huang,^{1,2} Andrew A. Wilson,^{1,2} Aditya Mithal,¹ Gustavo Mostoslavsky,¹ Irene Oglesby,^{3,4} Ignacio S. Caballero,¹ Susan H. Guttentag,⁷ Farida Ahangari,⁸ Naftali Kaminski,⁸ Alejo Rodriguez-Fraticelli,⁹ Fernando Camargo,^{9,10,11} Ziv Bar-Joseph,^{5,6,13,*} and Darrell N. Kotton^{1,2,13,14,*}

¹Center for Regenerative Medicine of Boston University and Boston Medical Center, Boston, MA 02118, USA

²The Pulmonary Center and Department of Medicine, Boston University School of Medicine, Boston, MA 02118, USA

³Department of Medicine, Royal College of Surgeons in Ireland, Education and Research Centre, Beaumont Hospital, Dublin, Ireland

⁴Tissue Engineering Research Group, Royal College of Surgeons in Ireland, Dublin, Ireland

⁵Computational Biology Department, School of Computer Science, Carnegie Mellon University, Pittsburgh, PA 15213, USA

⁶Machine Learning Department, School of Computer Science, Carnegie Mellon University, Pittsburgh, PA 15217, USA

⁷Department of Pediatrics, Monroe Carell Jr. Children's Hospital, Vanderbilt University, Nashville, TN 37232, USA

⁸Pulmonary, Critical Care and Sleep Medicine, Yale University School of Medicine, New Haven, CT 16520, USA

⁹Stem Cell Program, Boston Children's Hospital, Boston, MA 02115, USA

¹⁰Department of Stem Cell and Regenerative Biology, Harvard University, Cambridge, MA 02138, USA

¹¹Harvard Stem Cell Institute, Boston, MA 02115, USA

¹²These authors contributed equally

¹³Senior author

¹⁴Lead Contact

*Correspondence: zivbj@andrew.cmu.edu (Z.B.-J.), dkotton@bu.edu (D.N.K.)

<https://doi.org/10.1016/j.stem.2019.12.009>

SUMMARY

Alveolar epithelial type 2 cells (AEC2s) are the facultative progenitors responsible for maintaining lung alveoli throughout life but are difficult to isolate from patients. Here, we engineer AEC2s from human pluripotent stem cells (PSCs) *in vitro* and use time-series single-cell RNA sequencing with lentiviral barcoding to profile the kinetics of their differentiation in comparison to primary fetal and adult AEC2 benchmarks. We observe bifurcating cell-fate trajectories as primordial lung progenitors differentiate *in vitro*, with some progeny reaching their AEC2 fate target, while others diverge to alternative non-lung endodermal fates. We develop a Continuous State Hidden Markov model to identify the timing and type of signals, such as overexuberant Wnt responses, that induce some early multipotent NKX2-1⁺ progenitors to lose lung fate. Finally, we find that this initial developmental plasticity is regulatable and subsides over time, ultimately resulting in PSC-derived AEC2s that exhibit a stable phenotype and nearly limitless self-renewal capacity.

INTRODUCTION

A central aim of developmental biology is to better understand the embryonic differentiation and maturation pathways that

lead to functioning adult cells and tissues. Multistage, stepwise differentiation protocols applied to cultured human PSCs are designed to recapitulate these pathways in order to produce specific mature target cells. This approach allows the detailed *in vitro* study of the kinetics of human development at embryonic time points that are difficult to access *in vivo*, while also producing populations of cells for regenerative therapies and disease modeling. However, even the most optimized PSC differentiation protocols tend to yield a complex, heterogeneous mix of cells of varying fates and maturation states, limiting the successful recapitulation of target cell identity or purity (Schwartzentruber et al., 2018; Wu et al., 2018). This hurdle makes it challenging to understand the molecular mechanisms underlying human *in vivo* differentiation and consequently leads to limited clinical relevance and utility for several PSC-derived lineages.

The study of human lung development exemplifies this challenge. Access to developing fetal primary cells as experimental controls is limited, while *in vitro* differentiation of PSCs must attempt to recapitulate at least 20 weeks of gestational time that elapses from the moment of *in vivo* lung epithelial endodermal specification (approximately 4 weeks) until maturation of the earliest distal lung alveolar epithelial cells that exhibit surfactant producing organelles (24 weeks). We and others have published *in vitro* PSC-directed differentiation protocols that reduce the duration of this analogous *in vivo* developmental window to 2 weeks *in vitro* as PSC-derived lung endodermal precursors (NKX2-1⁺ primordial lung progenitors [PLPs] [Hawkins et al., 2017]) are differentiated in culture into lung alveolar epithelial type 2 cells (iAEC2s), the lifelong facultative progenitors of the alveolar epithelium (Gotoh et al., 2014; Huang et al.,

2014; Jacob et al., 2017). We have further shown that, despite sorting to purity for the earliest known lung progenitors, identified by NKX2-1 expression, during directed differentiation the resulting cells are plastic and transcriptomically heterogeneous and tend to drift over time into a variety of both lung and non-lung molecular phenotypes (McCauley et al., 2018). Importantly, this finding of fate heterogeneity mimics a variety of *in vivo* mouse developmental models or human lung cancer settings, which also document the emergence of ectopic endodermal programs in lung epithelial cells if signaling pathways, such as Wnt, or gene regulatory networks, such as those downstream of NKX2-1, are perturbed during key stages of fetal or adult life (Okubo and Hogan, 2004; Snyder et al., 2013; Tata et al., 2018). Given these results, detailed mapping of the developmental path or paths that progenitor cells take during differentiation to their end state or fate both *in vivo* as well as in PSC-derived systems has now become a primary objective of the field. Similar challenges in obtaining pure cell populations from PSC differentiation protocols were also recently observed for other tissue types such as the renal epithelium (Holtzinger et al., 2015; Schwartzenruber et al., 2018; Wu et al., 2018).

While single-cell RNA sequencing (scRNA-seq) can provide a detailed picture of cell states, distinguishing between immature and fully differentiated PSC-derived cells, this technique alone loses information about spatial and temporal factors and can only imply cell parent-progeny relationships in the absence of a lineage tracing strategy (Weinreb et al., 2018b). Several methods have been developed for inferring single-cell trajectories (Trapnell et al., 2014); however, these usually rely on dimensionality reduction, which makes it hard to infer the regulatory process that controls the branching of various cell fates (Ding et al., 2018).

To address these issues, here we present a general strategy for modeling such trajectories that can be used to better understand and improve differentiation protocols. We first employ bulk RNA sequencing of primary developing fetal and adult lung cells in order to map *in vivo* developmental maturation over time, establishing benchmark datasets and verifying key signaling pathways associated with maturation of the differentiated cells. Next, using a computational algorithm to interrogate the expression kinetics of a subset of genes profiled first at high resolution in differentiating PSCs, we select a set of optimal time points for global transcriptomic profiling and for these perform scRNA-seq time series analyses of PSC-derived cells. We use a novel computational method based on Continuous-State Hidden Markov models (CSHMMs) to construct developmental trajectories and to identify the regulators and pathways involved in controlling the process. We then use the computational model to predict both the *type* and *timing* of potential interventions, which can be used to increase the fraction of cells branching to the desired fate. We combine lentiviral barcoding with scRNA-seq to validate the parent-progeny lineage relationships and fate bifurcations predicted by our model. The outcome of these studies is a markedly improved understanding of the kinetics, fate trajectories, and cellular plasticity associated with PSC-directed differentiation, exemplified here by the derivation of lung alveolar epithelial cells from their developmental endodermal precursors.

RESULTS

Transcriptomic Profiles of Primary Human Developing Lung Alveolar Epithelium

We first sought to identify the transcriptional kinetics of maturation that characterize *in vivo* development of human AEC2s. We performed bulk RNA sequencing (RNA-seq) of distal human fetal and adult lung alveolar epithelium at 3 key developmental time points (Figure 1A). Using our previously published methods (Gonzales et al., 2002; Jacob et al., 2017; Wade et al., 2006), we purified alveolar epithelial cells from human fetal lungs (HFLs) at 16–17.5 weeks of gestation ($n = 3$; hereafter early HFLs), 20–21 weeks of gestation ($n = 4$; hereafter late HFLs), and postnatally from adult lungs ($n = 3$). These three time points represent, respectively, (1) early canalicular-staged cells composed of distal lung bud tip epithelial cells that are thought to have already initiated their alveolar programs (Miller et al., 2018; Nikolić et al., 2017, 2018); (2) more differentiated alveolar cells at a later canalicular stage but just prior to the emergence of lamellar bodies (Nikolić et al., 2017); and (3) fully mature adult AEC2s, sorted based on HTII-280 expression (Jacob et al., 2017). To enable comparison of these samples to an earlier staged NKX2-1⁺ lung endodermal progenitor, we also profiled *in vitro* PSC-derived PLPs ($n = 3$), sorted using previously published surface markers (CD47^{hi}/CD26^{neg}) (Hawkins et al., 2017). At a false discovery rate (FDR) <0.05 (empirical Bayes ANOVA test), we identified 15,137 differentially expressed genes across the 13 samples, in line with recent studies that found that a large portion of the transcriptome is differentially expressed in early development (Cao et al., 2019).

To focus on a smaller number of genes, we selected the 1,000 genes with the highest variance in expression across all 13 samples in order to identify transcripts most associated with early human alveolar differentiation versus maturation (Figures 1B and 1C). Hierarchical clustering of these genes identified candidate “differentiation” clusters, which included a cluster that varied early in alveolar development (weeks 16–21) and a “maturation” cluster enriched preferentially in adult AEC2s (Figure 1C). We plotted the expression kinetics of cluster genes to select 8 markers of early distal alveolar differentiation that are expressed during fetal canalicular stages prior to full AEC2 maturation (“differentiation” gene set: SFTPB, SFTPC, SFTPD, CLDN18, LAMP3, SLC34A2, IL8, and NAPSA; Figure 1D). Next, we identified a 6 gene “maturation” marker set, LYZ, SFTPA1, SFTPA2, PGC, CXCL5, and SLPI, which was preferentially expressed in adult AEC2s. We further identified genes downregulated in adult AEC2s (MYCN, SOX11, and the Wnt target genes, NKD1, NKD2, and LGR5; Figure 1D). Based on prior literature (Frank et al., 2016; Hogan et al., 2014; Jacob et al., 2017), and significant differential expression between primary fetal and adult AEC2s, we also selected downregulation of Wnt targets LEF1 and BAMBI and the transcription factor (TF) SOX9 as additional stage-dependent maturation markers of AEC2s, although SOX9 variance was not in the top 1,000 varying genes overall. Taken together, our profiles indicate the early development of distal human lung epithelium is characterized by the expression of a subset of surfactant- and lamellar body-associated genes, some of which increase non-linearly

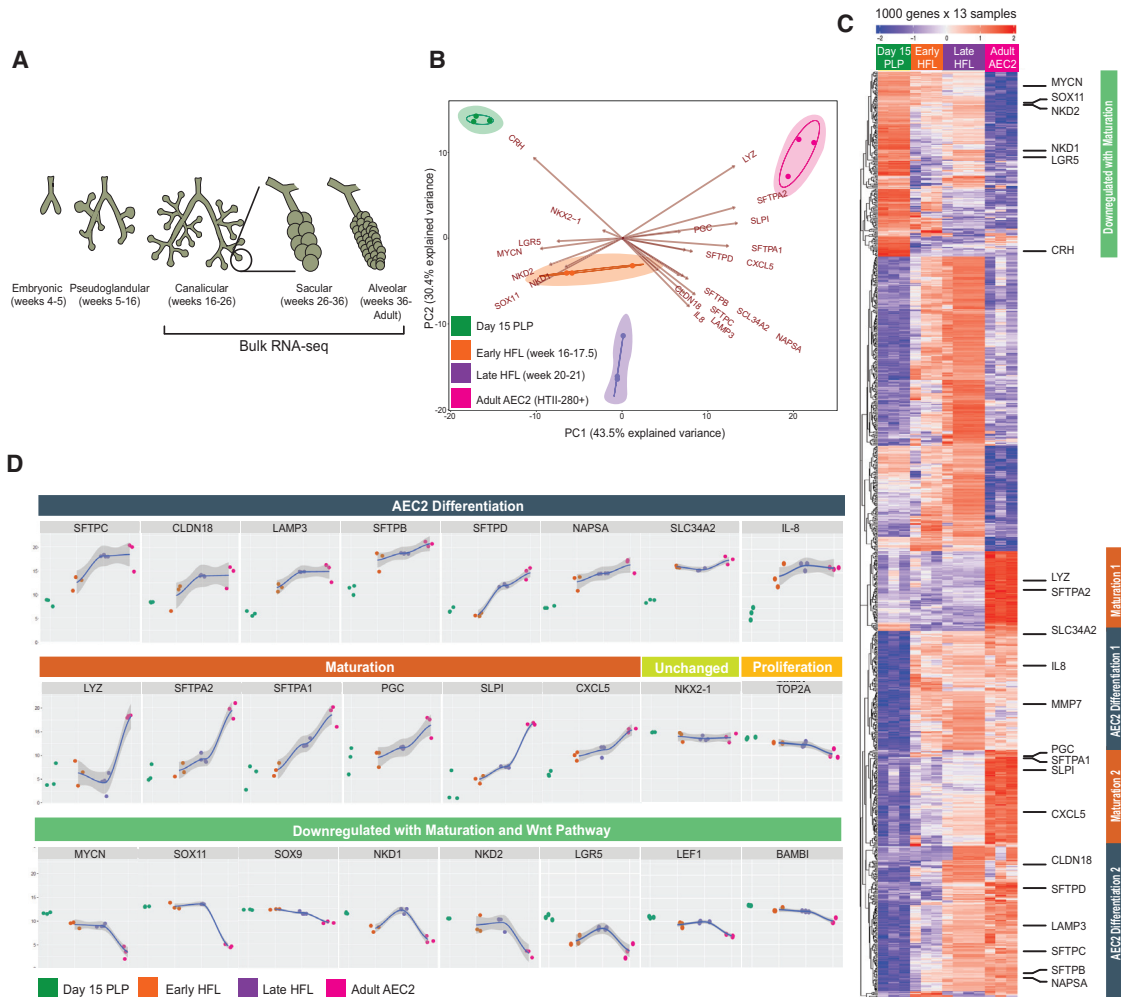


Figure 1. Global Transcriptomic Time Series Reveals the Kinetics of Developing Primary Human Alveolar Epithelial Type 2 Cells

(A) The 5 stages of human lung development and samples obtained for bulk RNA sequencing.

(B) Principal-component analysis (PCA) of gene expression across all 13 samples including primordial lung progenitors (PLPs) derived from pluripotent stem cells at day 15 of differentiation, primary early human fetal lung alveolar epithelium (HFL; 16–17.5 weeks gestation), late HFL alveolar epithelium (20–21 weeks gestation), and adult alveolar epithelial type 2 cells (AEC2) sorted on the antibody HTII-280. The loadings of highly variable genes associated with differentiation and maturation of AEC2 in (C) are overlaid on the PCA plot in B to indicate their weight on PC1 and PC2. Arrow tips denote the correlation coefficient of the respective gene with each principal component.

(C) Heatmap showing unsupervised hierarchical clustering of the top 1,000 most variable genes across all samples.

(D) Smoothed regressions of time series samples indicating normalized gene expression values (from C) for 8 selected genes associated with differentiation of AEC2, 6 genes associated with maturation of AEC2 and 8 selected downregulated AEC2 maturation and Wnt pathway genes.

See also [Table S1](#).

over time (Figures 1C and 1D), followed by the later expression of genes associated with AEC2 maturation, including expression of the full complement of surfactant proteins and additional markers that others have observed in adult AEC2s (Desai et al., 2014; Treutlein et al., 2014; Guo et al., 2019). Conversely, maturation of AEC2s is associated with decreasing Wnt signaling consistent with prior findings *in vivo* in mice (Frank et al., 2016) as well is *in vitro* in iAEC2s (Jacob et al., 2017). In contrast, the canonical TF required for lung epithelial development, NKX2-1, maintains its expression over time (Figure 1D) in developing iAEC2s, supporting its utility as a marker expressed throughout the lifetime of AEC2s.

Selecting the Most Appropriate Time Points to Profile in a scRNA-Seq Analysis

Using the markers identified from profiling the transcriptomic kinetics of primary alveolar epithelial differentiation, we next sought to determine whether the differentiation trajectories of PSC-derived cells truly recapitulate human lung developmental kinetics. We employed our recently published protocol (Jacob et al., 2017), differentiating purified PSC-derived primordial NKX2-1⁺ lung progenitors over a 2-week period into iAEC2s. This prolonged time needed to differentiate human iAEC2s presents a substantial problem in selecting the number of developmental time points to exhaustively profile using

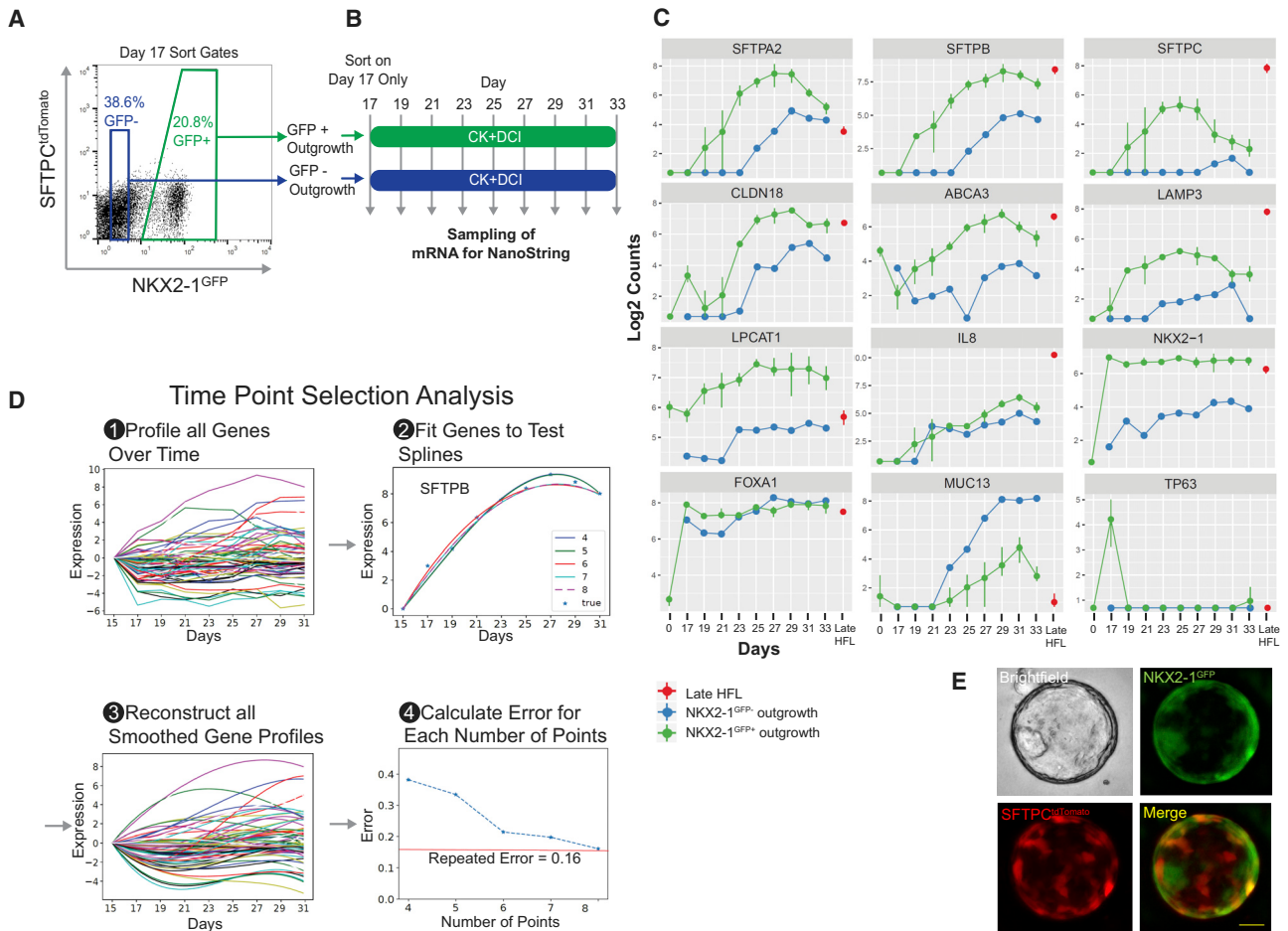


Figure 2. Time Point Selection Analysis of Lung Differentiation by NanoString Predicts Optimal Time Points for Global Transcriptomic scRNA-seq Profiling

(A) Representative sort gates of iPSCs sorted on NKX2-1^{GFP+} versus NKX2-1^{GFP-} on day 17 of differentiation. (B) Schematic of differentiation protocol after fluorescence-activated cell sorting (FACS) at day 17 with outgrowths cultured in CK⁺DCI media and sampled at time points shown. (C) Average and range of expression over time for selected genes (0–33 days of differentiation, n = 3 biological replicates). Red dot indicates late human fetal lung alveolar epithelial controls (HFLs; 20–21 weeks gestation). (D) Schematic of TPS method for choosing the optimal time points for the single-cell experiment, iteratively evaluating the effect of removing time-points on the overall error until an optimal is found. (E) A representative self-renewing monolayered epithelial sphere composed of iAEC2s co-expressing GFP and tdTomato. Scale bar, 50 μm.

costly methods such as scRNA-seq. The question of when and how often to sample is particularly challenging in developmental *in vitro* models, as molecular changes are likely non-linear, so simple linear sampling may fail to identify significant gene fluxes (Li et al., 2013). To address this issue, we adapted an algorithm we previously developed for the task of selecting optimal time points to profile in scRNA-seq studies using bulk data containing gene subsets. Our algorithm, time point selection (TPS) (Kleyman et al., 2017), profiles a small set of selected genes sampled at a high rate. These are represented using splines and a combinatorial search is applied to select a subset of suitable points so that combined, selected points provide enough information to reconstruct the values for all genes across all time points (including those not selected, Figure 2A-D). The final number of points to be used can be

determined as a function of the reconstructed error. To use TPS, we profiled 80 relevant differentiation and maturation genes in PSC-derived differentiation to iAEC2s, every 2 days, over a 16-day period by NanoString (Figure 2B). Genes were selected from our *in vivo* analysis discussed above and from prior endodermal profiling (Hawkins et al., 2017) (Table S1; Figure S1). For these studies, we utilized a non-diseased induced pluripotent stem cell (iPSC) line (BU3 NGST) that we have engineered to carry knockin fluorescent reporters (NKX2-1^{GFP}; SFTPC^{tdTomato}) allowing real-time monitoring of cells as their cell states proceed from initial lung specification (NKX2-1^{GFP+}) through their differentiation into NKX2-1^{GFP+}/SFTPC^{tdTomato+} iAEC2s (Jacob et al., 2017). We separated lung from non-lung cells at the primordial progenitor stage (based on GFP⁺ versus ⁻ sorting; Figure 2A) and profiled

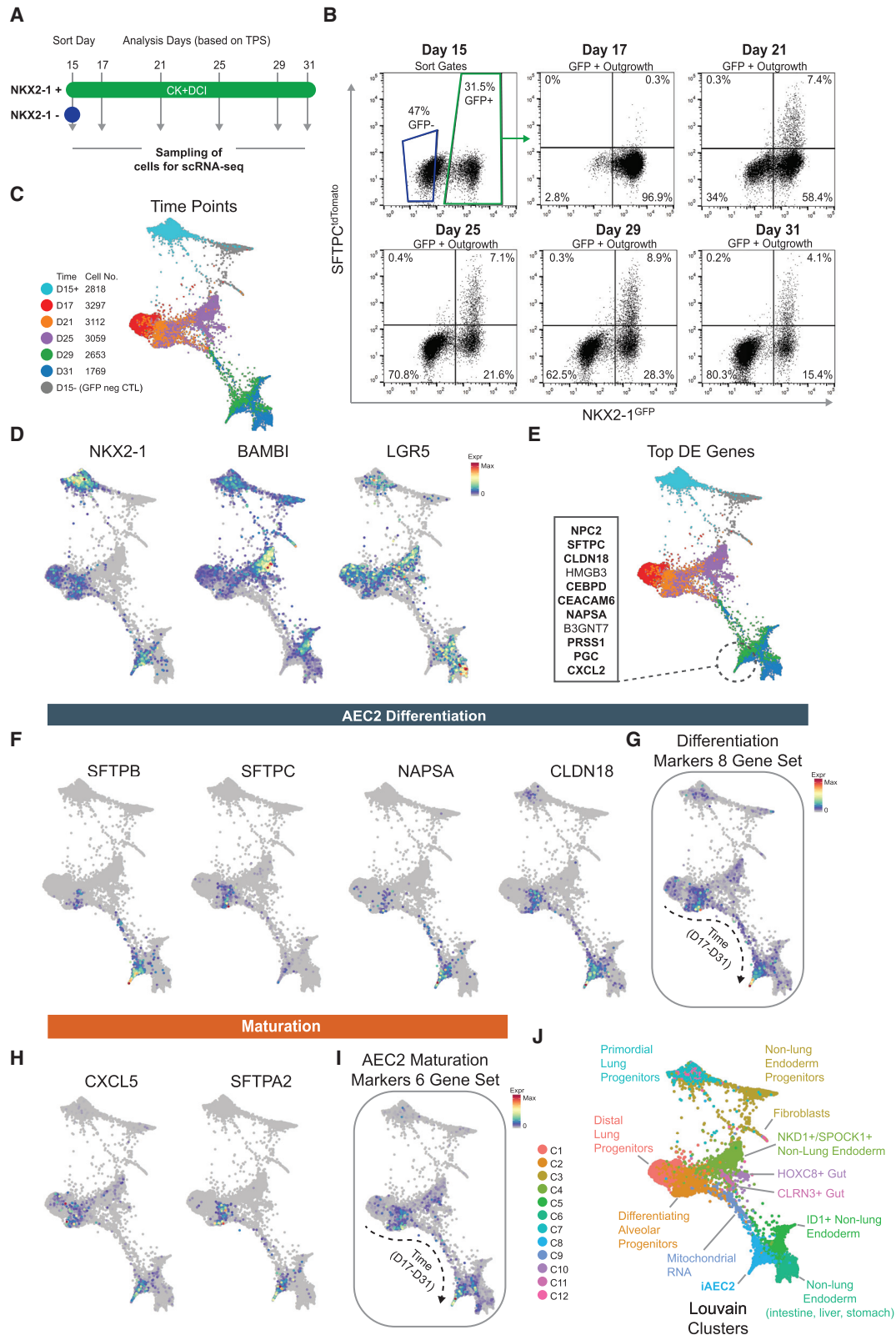


Figure 3. Time Series Single-Cell Transcriptomic Analysis of AEC2-Directed Differentiation

(A) Schematic of experiment indicating sorting of iPSC-derived PLPs (day 15) and analysis of their outgrowths over time.

(B) Flow cytometry analyses at the time of cell capture for each scRNA-seq.

(legend continued on next page)

the outgrowth of the GFP⁺ versus GFP⁻ populations without further cell sorting (Figure 2C; Figure S1).

For this small panel, we observed that expression of surfactant-encoding and lamellar body-related genes, SFTPB, SFTPC, SFTPA2, ABCA3, and LAMP3, increased over time to a maximum at days 25–29 and decreased thereafter (Figure 2C), while NKX2-1 remained constant. As expected, lung epithelial markers were relatively depleted in the outgrowth of GFP negative controls, consistent with our prior reports that all PSC-derived human lung epithelial lineages derive via the gateway of an NKX2-1⁺ primordial progenitor stage (Hawkins et al., 2017; Jacob et al., 2017; McCauley et al., 2017, 2018; Serra et al., 2017). TPS identified an inflection point when using the optimal 6 time points (days 15, 17, 21, 25, 29, and 31). While error increased rapidly when using less than 6 points, 7 or more points did not significantly reduce reconstruction error. As seen in Figure 2D, for the optimal set of 6 points, the reconstruction error is close to the repeat error suggesting accurate inference of non-profiled time points.

A Single-Cell Map of PSC-Derived Distal Lung Differentiation Implies Fate Trajectories

We next profiled the transcriptional trajectories of individual cell states over time by scRNA-seq performed at the time intervals selected by our TPS algorithm (Figure 3A). For each time point, we profiled ~4,000 cells, following PSC-derived cells sorted on NKX2-1^{GFP} at the lung primordial progenitor stage of differentiation (day 15; Figure 3B) through day 31 of alveolar-directed differentiation without further sorting. As a negative control, we included a 7th sample, the day 15 non-lung population, isolated based on GFP exclusion (NKX2-1^{GFP} negative sorted). Flow cytometry monitoring of NKX2-1 and SFTPC locus activity at each of the 6 time points of alveolar differentiation (Figure 3B) indicated the expected emergence of SFTPC^{tdTomato} expression over time in some cells, peaking on day 29 of differentiation but a loss of NKX2-1^{GFP} expression in other cells over time, predicting potential loss of lung cell fate in a subset of the population, consistent with our prior report (McCauley et al., 2018).

To visualize potential single cell-fate trajectories in our model while preserving high-dimensional relationships, we first utilized the SPRING algorithm (Weinreb et al., 2018a) to prepare forced-directed layouts of k-nearest neighbor graphs for the entire differentiation time series (Figure 3C). GFP⁺- and GFP⁻-sorted populations at the starting day 15 time point were easily distinguished based on NKX2-1 transcript expression levels (Figure 3D), validating the efficacy of the NKX2-1^{GFP} reporter. Furthermore, the outgrowth of the GFP⁻-sorted population could be visualized on SPRING plots as adjacent populations ordered sequentially in time. Apparent bifurcations appeared as multiple branchpoints in transcriptomic trajectories after day 17 (Figure 3C) possibly implying branching cell fates over time, with

distinct branches to lung (NKX2-1 positive) and non-lung fates (NKX2-1 negative; BAMBI⁺ and LGR5⁺), spread over multiple time points (Figure 3D). Trajectories where NKX2-1 expression was maintained after day 17, exhibited subsequent surfactant-encoding and lamellar body-encoding gene expression, beginning on day 21, consistent with a time-dependent alveolar epithelial differentiation program (Figures 3E–3H). We used the mature AEC2 marker profiles identified in primary cells (Figure 1), and we found cells with expression for these markers in late branching parts of the plot representing day 29–31 time points (Figures 3E and 3H). Eight out of the top 10 most upregulated transcripts in this branch (Figure 3E) were known AEC2 genes that were also present in our primary adult AEC2 differentiation and maturation sets (Figures 1C and 1D) including SFTPC, CLDN18, CEBP δ , NAPSA, and PGC. Taken together, these results are consistent with a fate trajectory followed by a subset of iPSC-derived NKX2-1⁺ lung progenitors, only some of which reach mature AEC2-like states over a 2-week period.

A Continuous Branching Network Model Learns, Predicts, and Maps Cell-Fate Paths

Since the SPRING analysis provides a low dimensional dynamic representation implying branching trajectories, we next sought to fully reconstruct these putative branching points to study their regulation and to characterize the set of TFs and signaling pathways associated with their potentially bifurcating fates. For this, we extended our previously developed computational method based on Hidden Markov models (HMMs) (Ding et al., 2018; Rashid et al., 2017) in order to continuously assign cells along trajectories while still being able to infer regulators controlling branching events, hereafter referred to as a CSHMM (see STAR Methods). This model allowed us to combine the continuous representation offered by current dimensionality reduction methods with the ability to handle noise and dropouts and identify regulators based on its probabilistic assumptions (Lin and Bar-Joseph, 2019). Unlike standard HMMs, which are defined using a discrete set of states, CSHMMs can have infinitely many states allowing for continuous assignment of cells along developmental trajectories. A schematic of the learning procedure is depicted in Figure 4A (see STAR Methods for details) resulting in the paths (PO–10) and nodes (NO–11) of a differentiation tree representation, which is not evident when using conventional methods such as t-Distributed Stochastic Neighbor Embedding (tSNE) plots (Figure S2).

To test whether the model indeed captures paths corresponding to human lung development, we first compared the reconstructed CSHMM map to our human *in vivo* expression data by projecting global gene expression from our 4 developmentally relevant time points (PLP, early HFL, late HFL, and adult AEC2, Figure 1) onto the CSHMM map (Figures 4A–4C). The best correlation between the model and the *in vivo* expression data

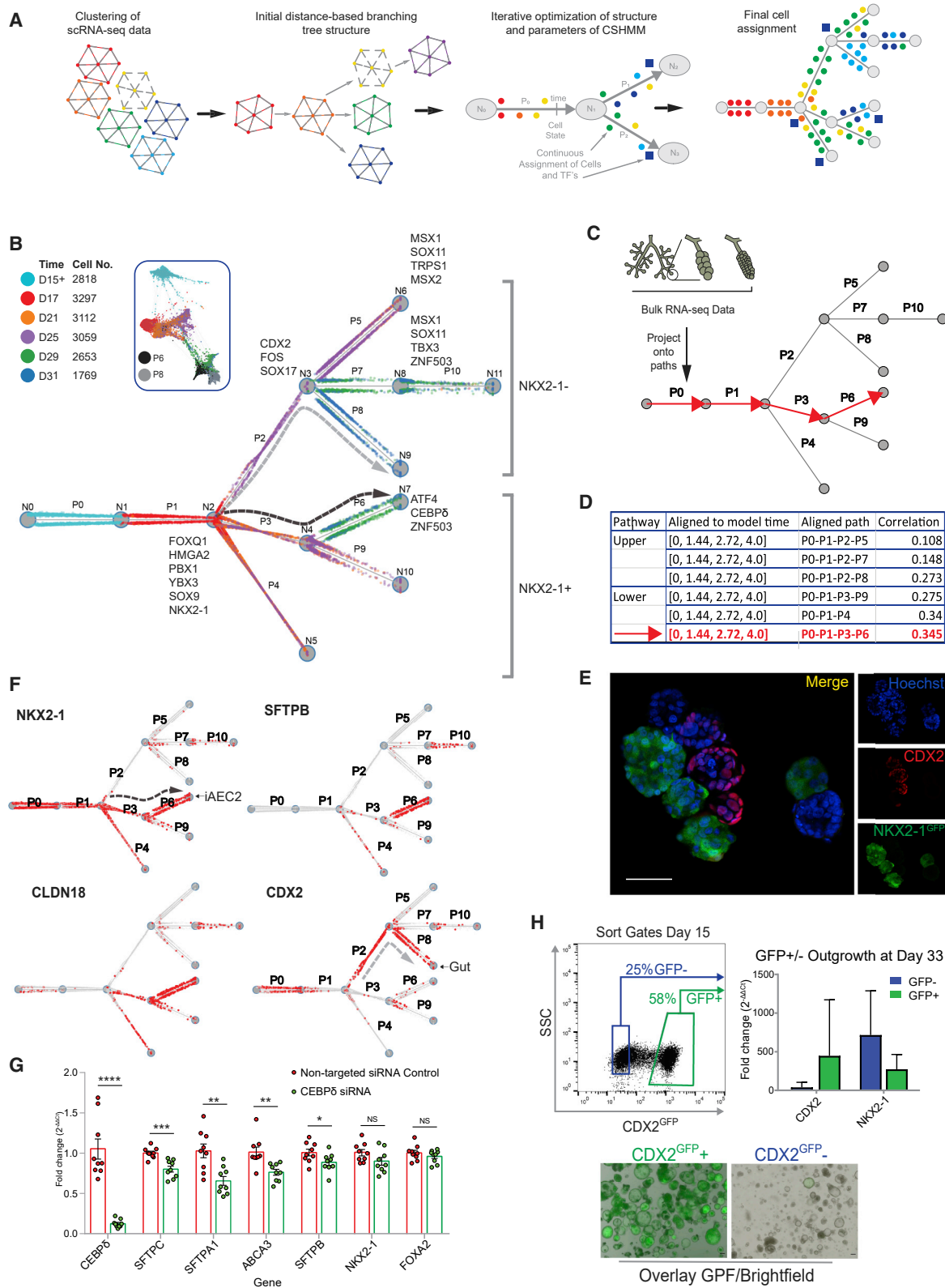
(C) SPRING analysis of all cells from (B) across all 6 time points. “D15-” represents the NKX2-1^{GFP} negative control shown in (A), sorted on day 15.

(D) Normalized gene expression overlaid on SPRING plots for selected markers of retained lung fate (NKX2-1) versus BMP and Wnt signaling markers.

(E) The top 11 transcripts upregulated in cells in the indicated gate compared to all other cells; bold font indicates a known marker of AEC2s. DE=differentially expressed.

(F–I) Normalized expression levels for selected AEC2 marker genes as well as the composite set (G) of 8 AEC2 differentiation markers or 6 AEC2 maturation markers (H and I) from Figure 1.

(J) Louvain clustering with identities assigned based on markers explained in the text or indicated in the panel. See also Figure 1 and Figure S2.



(legend on next page)

was achieved for the P0-P1-P3-P6 path, which leads to AEC2-like cells (Figure 4C, bottom path). More generally, correlations with bottom paths that lead to AEC2-like cells were 20% higher than those with the top paths indicating that for multiple branches *in vitro*, PSC-derived differentiation data are in good agreement with *in vivo* data (Figure 4D). To allow seamless comparisons between CSHMM and SPRING plots, we developed an interactive web tool (<http://cosimo.junding.me>). Using this tool, we found that the P0-P1-P3-P6 CSHMM path matched the implied SPRING trajectory to the mature AEC2 cluster (Figure S2).

Next, we sought to use our reconstructed model to determine when cell fates begin to diverge (Figure 4B). The reconstructed CSHMM model depicted a split in cell fate after day 17, with 6,202 cells assigned to the non-lung endoderm (top) paths and 5,980 cells assigned to lung (bottom) paths. The top path, P1-P2-P8 (Figure 4B), was enriched for the expression of intestinal cell marker (CDX2), while the bottom path, P1-P3-P6, was enriched for the expression of lung epithelial markers, such as NKX2-1, CLDN18, and SFTPB (Figures 4B, 4D, and 4E). Similar to the intestinal path, additional top non-lung paths, P2-P5 and P2-P7, were found to be endodermal (FOXA1⁺, FOXA2⁺, and some SOX17⁺), epithelial (EpCam⁺, CDH1⁺), and not lung (NKX2-1 negative). However, their identities did not match any known *in vivo* tissue identity gene sets; thus, they were named based on 1–2 markers highly enriched in each of these non-lung endodermal (NLE) paths (Table S2), namely, NKD1⁺/SPOCK1⁺ NLE for P2-P5 and ID1⁺ NLE for P2-P7 (Figures S2B and S2G). Cells in the P10 path were those not assigned to either of these two fates, and top differential genes in these cells were mostly mitochondrial genes (see Table S2 for the complete DE gene list for each path).

The model identified several TFs putatively regulating each of the predicted paths at branching points (Figure 4B). TFs assigned to the first major fate split are known regulators for lung epithelial fate including the distal lung developmental regulator SOX9 (Perl et al., 2005; Rockich et al., 2013) and HMGA2, a TF highly expressed in human distal lung bud tip cells (Nikolić et al., 2017) and lung epithelial carcinomas (Snyder et al., 2013). We have previously suggested that HMGA2 plays a role in mouse distal lung epithelial development based on analyses of the global transcriptomes of lung tissues from E18.5

HMGA2 knockout mice (Ding et al., 2018). For the bottom lung epithelial path to iAEC2 fate (P3–P6, black arrow), the model identified ATF4, CEBP δ , and ZNF503 as top TFs most associated with iAEC2 fate, findings in keeping with recent analyses of newborn lungs where CEBP δ and ATF4 are TFs highly expressed in the alveolar epithelium *in vivo* at post-natal day 1 (Guo et al., 2019). We performed small interfering RNA (siRNA)-based knockdown of CEBP δ in iPSC-derived iAEC2s and found this resulted in reduced SFTPC, SFTPB, ABCA3, and SFTPA1 gene expression levels without altering endodermal (FOXA2) or lung TF (NKX2-1) levels (Figure 4F) consistent with a role for CEBP δ in maintenance of the AEC2-specific program. The branching model also predicted that CDX2, FOS, and SOX17 are top TFs associated with the non-lung endoderm or intestinal fate paths (P2–P8, gray arrow), and we validated this finding in independent experiments using another iPSC line (BU1 carrying a CDX2^{GFP} knockin reporter; Mithal et al., 2020) observing that sorted CDX2^{GFP+} cells at day 15 of our lung differentiation protocol were markedly enriched in intestinal competence, in contrast to CDX2^{GFP-} negative cells, which were enriched for lung competence and depleted for intestinal competence (Figure 4G).

CSHMM Predicts the Precise Timing of Wnt Modulation that Maintains Lung Cell Fate

In addition to TFs, the branching identified by the CSHMM model assigned cells in which the Wnt and BMP signaling pathways were upregulated in the progeny of sorted NKX2-1^{GFP+} cells as they diverged to the non-lung paths (Figures 5A and S3). Specifically, 4 of the 5 top differentially expressed genes in the NLE (top) path were related to Wnt signaling: WIF (Ng et al., 2014), HIPK2 (Tan et al., 2014), NEAT1 (Zarkou et al., 2018), and THBS1 (Han et al., 2014) (Table S2). Furthermore, Wnt target genes LEF1, NKD1, and AXIN2 (McCauley et al., 2017) were all upregulated in cells following non-lung paths, compared to those maintaining lung paths. We and others have observed that downregulation of Wnt signaling targets has stage-dependent effects in lung development *in vivo* (Frank et al., 2016; Mucenski et al., 2003; Shu et al., 2005) and *in vitro* (Jacob et al., 2017; McCauley et al., 2017), inducing proximal airway patterning when downregulated at the NKX2-1⁺ primordial progenitor stage (PSC differentiation day 15), whereas

Figure 4. Fate Trajectories Predicted Based on a Continuous-State Hidden Markov Model

- (A) Schematic summarizing the CSHMM method (detailed in STAR Methods).
 (B) The resulting CSHMM model for lung-directed differentiation. Each dot represents a cell; color denotes the time point in which the cell was sampled. Nodes are denoted by N0, N1, etc. while branches (paths) are denoted by P0, P1, etc. (note that several branches can share a node). Names next to paths are the transcription factors (TFs) that are differentially expressed for these paths.
 (C and D) Alignment of bulk RNA-seq data from 4 *in vivo* time points (Figure 1) was projected onto the CSHMM model paths and is shown in C. The correlation of expression values between the bulk time series data and all possible set of paths in the model was computed and is shown in table D.
 (E) Representative confocal fluorescence micrograph of epithelial sphere outgrowth from NKX2-1^{GFP+} progenitors sorted on day 14 and cultured until day 35 of differentiation. Immunostaining for cytoplasmic GFP (green) and nuclear CDX2 (red) protein indicates distinct cells express these lung versus hindgut markers (blue, Hoechst DNA counterstain; scale bar, 200 μ m).
 (F) Expression of specific markers in cells assigned by CSHMM to different branches. For example, SFTPB-expressing cells are mainly assigned to P6, whereas NKX2-1 cells are assigned to all paths leading to P6.
 (G) Relative expression levels of each indicated AEC2 or endodermal transcript (RT-qPCR) in iAEC2s after knockdown of CEBP δ by siRNA.
 (H) First panel: sort gates for iPSC line carrying a CDX2^{GFP} reporter, on day 15 were used to purify CDX2^{GFP+} versus CDX2^{GFP-} cells. Second panel: after outgrowth of each sorted population in identical media, the relative gene expression levels on day 33 are shown for CDX2 and NKX2-1. Representative bright-field and fluorescence microscopy overlays indicate levels of CDX2^{GFP} fluorescence on day 33 of outgrowth resulting from each indicated population sorted on day 15.

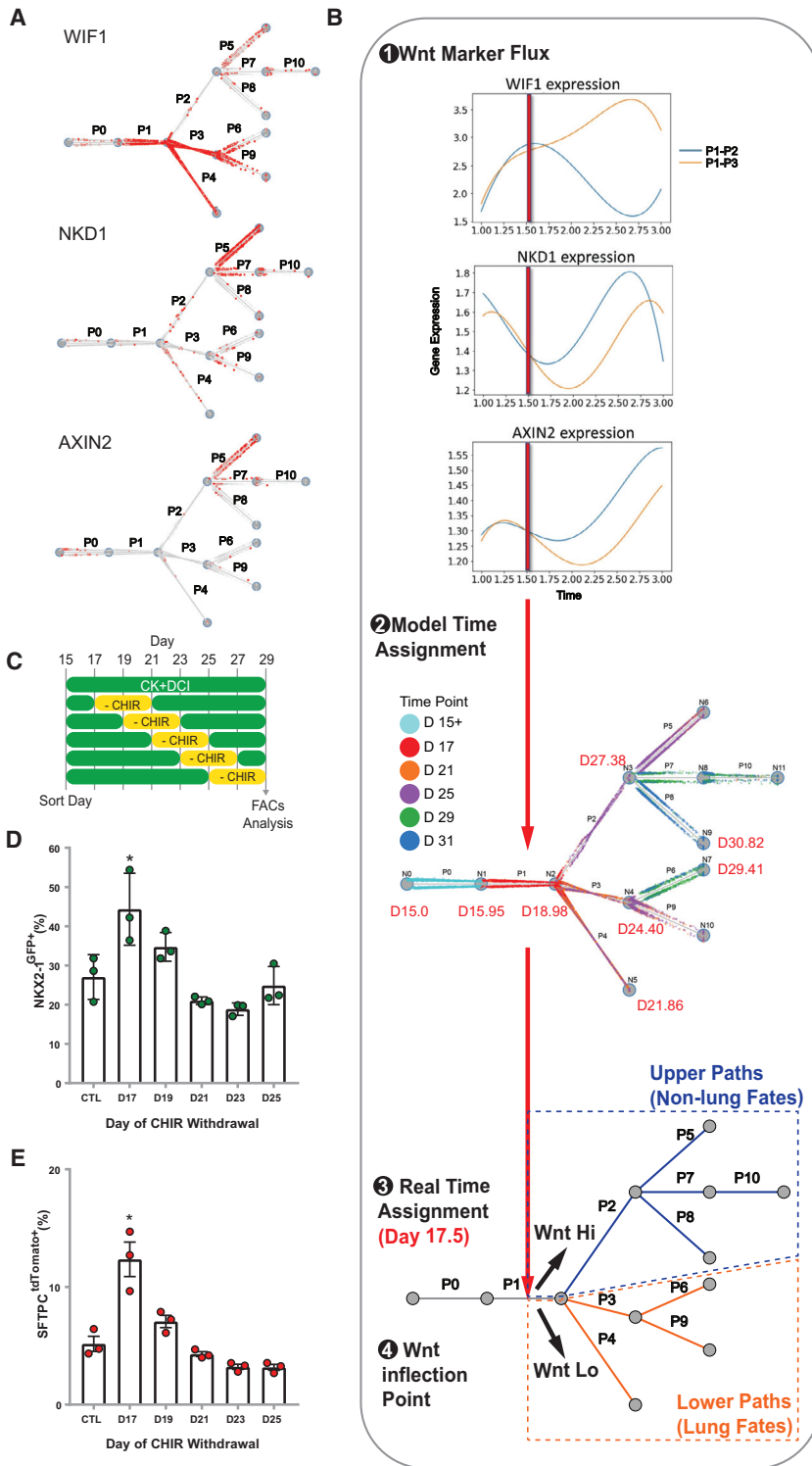


Figure 5. CSHMM Predicts the Precise Timing of Wnt Modulation as a Determinant of Cell Fate

(A) Expression of key Wnt target genes overlaid on CSHMM showing enrichment in top versus bottom paths.

(B) Schematic of method used to determine the exact time of Wnt pathway activation. The top 3 panels show the continuous expression of Wnt markers reconstructed using splines for the top paths (blue curve) versus bottom paths (orange curve). For all three markers, there is a split in expression values at the halfway point between nodes N1 and N2 (middle of P1). To determine the real time denoted by this point, a time is assigned for each node in the CSHMM tree revealing that the middle point is day 17.5.

(C) Schematic summarizing experimental plan for testing effect of time-dependent downregulation of canonical Wnt signaling by CHIR withdrawal.

(D and E) Retention of distal lung epithelial fate on day 29 of the experiment described in (C), measured by the frequency of cells expressing the (D) NKX2-1^{GFP} and (E) SFTPC^{tdTomato} reporters quantified by FACS. *ANOVA $p < 0.05$.

Therefore, we used the reconstructed branching model to predict the optimal time point for Wnt withdrawal in order to maximize the set of cells maintaining lung fate in our protocol. To find that point, we selected a set of canonical Wnt signaling target genes and plotted their expression in the lung and non-lung trajectories. As can be seen in Figure 5B, these genes start to diverge at the mid-point of P1. To assign an actual time to that point, we looked at cells assigned by CSHMM before and after that midpoint and computed the average time in which these cells were profiled. Using this, we determined that day 17.5 (red arrow in Figure 5B) is the time of split between the two branches. To test this prediction, we repeated our directed differentiations while withdrawing CHIR from our media for a period of 4 days (Figure 5C), starting at five different time points over the 2-week period of differentiation of sorted NKX2-1^{GFP+} lung progenitors toward the desired iAEC2 target (days 15–29). To maintain proliferation of resulting cells, CHIR was added back after 4 days, allowing each parallel condition to be harvested at the identical total differentiation time while keeping the length of CHIR withdrawal (4 days) constant for each condition.

downregulation in distal lung epithelium *in vivo* (Frank et al., 2016) or in iAEC2s (Jacob et al., 2017) at later stages is associated with distal lung maturation, as validated in our human primary cell RNA-seq (Figure 1). However, the optimal timing of downregulation of Wnt, for example, by withdrawal of the GSK3 inhibitor, CHIR, in our system has not been established.

As predicted by the model, withdrawal of CHIR beginning on day 17 resulted in the highest rates of retention of distal lung epithelial fate as quantified by flow cytometry measurement of NKX2-1^{GFP} and SFTPC^{tdTomato} reporter expression on day 29 (Figures 5D and 5E). Overall, these experiments demonstrate that CSHMM not only can identify the relevant signaling

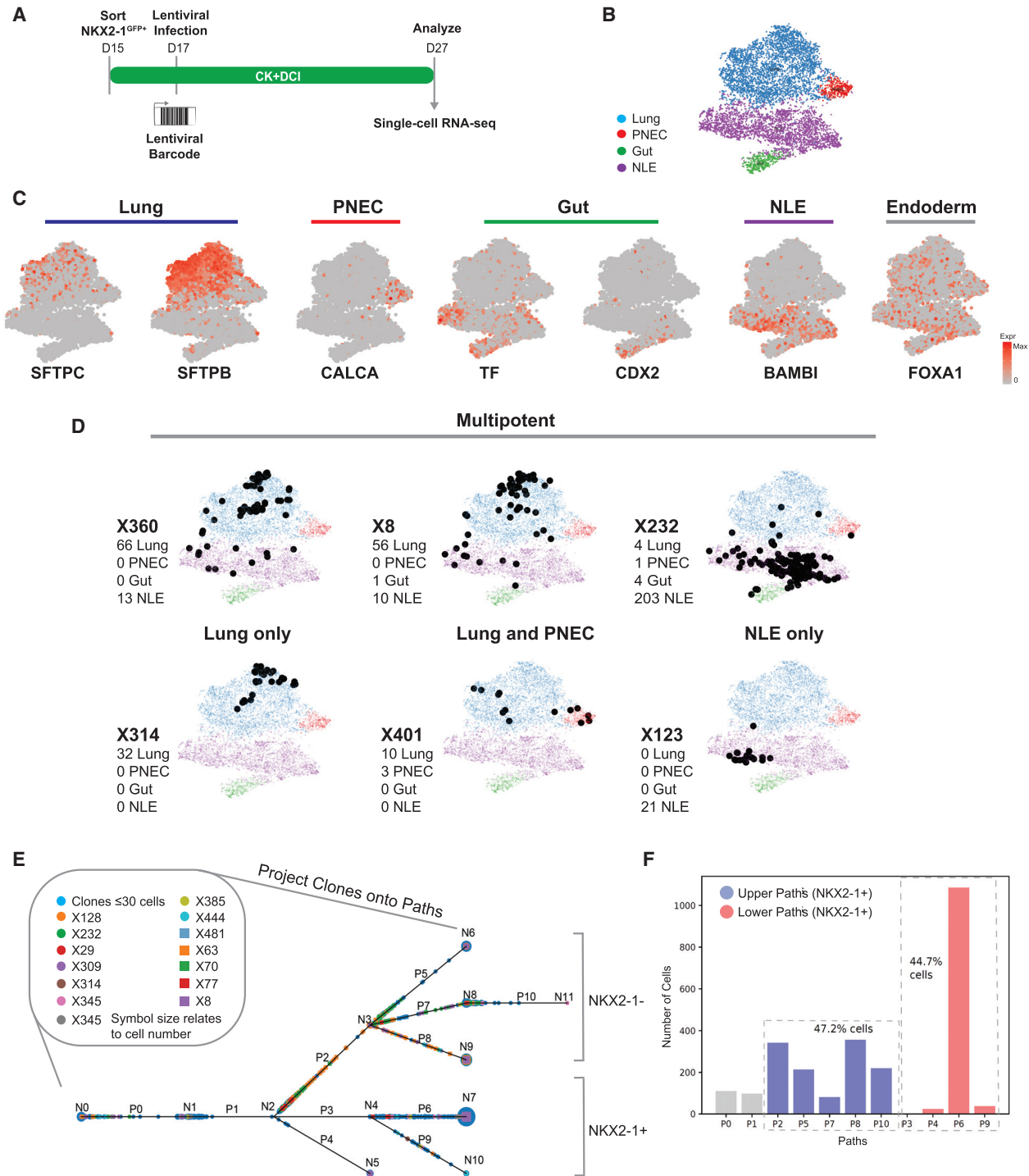


Figure 6. Lineage Tracing Using Lentiviral Barcoding Reveals Clonal Heterogeneity

(A) Schematic of experiment showing infection of NKX2-1⁺ outgrowth at day 17 with lentivirus to tag progenitors with unique integrated DNA barcodes. Replated cells were cultured in 3D Matrigel for a further 10 days. Inherited lentiviral barcodes were matched with transcriptomic profiles for each cell by scRNA-seq to track clones.

(B) tSNE plot of all cells harvested at day 27 with Louvain clusters annotated based on marker genes for distal lung alveolar epithelium “lung”, pulmonary neuroendocrine cells (PNECs), gut, and non-lung endoderm (NLE).

(C) Normalized gene expression overlaid on tSNE plots for selected markers.

(legend continued on next page)

pathways that determine cell fate in our system but can also predict with precision the timing of pathway modulation to increase differentiation efficiency to the target cell.

We validated the emergence of divergent cell fates predicted by our model, by comparing findings from our CSHMM to 2 additional computational methods for the detection of fate bias or fate entropy, FateID (Herman et al., 2018) and WaddingtonOT (Schiebinger et al., 2019) with similar conclusions (Figure S4).

Lineage Tracing Using DNA Barcoding Reveals Clonal Heterogeneity and Fate Plasticity

The CSHMM computationally predicts multipotency at least until day 17.5, with some cells branching to lung and others to non-lung after this time. To functionally test this prediction, we employed lentiviral barcoding to clonally trace the progeny of individual cells in the protocol followed by scRNA-seq profiling to assign them to paths in the model. On day 15 of differentiation, PSC-derived NKX2-1 progenitors were sorted to purity, and on day 17 a single-cell suspension of these progenitors was infected with our lentiviral barcoding library for “Lineage and RNA Recovery” (LARRY) (Weinreb et al., 2020), which encodes for enhanced green fluorescent protein (eGFP) mRNA together with a 3' UTR carrying a unique inheritable barcode for each cell (Figure 6A). This library has a complexity of 10^6 barcodes, sufficient to label 10^4 cells with <0.5% barcode overlap between clones (Weinreb et al., 2020). We first optimized this system to achieve a transduction efficiency in iPSC-derived lung progenitors of ~30% using a viral multiplicity of infection (MOI) = 10. Following lentiviral infection of 32,500 progenitors on day 17, both the infected cells and parallel uninfected (MOI = 0) control progenitors were cultured for an additional 10 days in our distal lung media prior to capture for scRNA-seq (Figure 6A). Analysis of the single-cell transcriptomes of 6,147 cells from the MOI = 10 condition and 1,644 cells from the MOI = 0 control revealed four cell states or clusters (Figure 6B). Comparing infected (MOI = 10) to uninfected (MOI = 0) samples by tSNE plots revealed an overlap of all 4 clusters, indicating that lentiviral infection and tagging did not detectably perturb differentiation (Figure S5). We annotated the 4 cell clusters, based on the expression of identity marker genes as distal lung epithelium (hereafter “lung”) and “non-lung endoderm” and 2 minor clusters: pulmonary neuroendocrine cells (PNECs) and “gut” (Figures 6B and 6C; Table S3 for full list).

We identified all lentivirally transduced clones within each cell cluster by associating lentiviral barcodes to cell transcriptomes (Figure 6; Table S4). We identified 487 unique clones with 45 clones containing more than 10 cells per clone (Figure S5). The majority of these 45 clones contained cells that were found in more than one cell state (23/45 contributing to both lung [lung or PNEC] and non-lung [NLE or gut] clusters; Figure 6D; Figure S5). For example, the largest clone X232 (212 cells) was found to contribute progeny to all 4 cell clusters implying that

at least a subset of day 17 parental progenitors was likely following the bifurcating tree predicted by CSHMM.

We next directly overlaid barcoded cells on the CSHMM fate maps (Figure 6E). Given experimental differences in profiling cells used to construct the CSHMM model and barcoded cells, we projected barcoded cells using a subset of 82 genes, including the top 68 genes differentially expressed between the top and bottom paths (P2 and P3) and 14 distal lung markers from our primary cell datasets (Table S5). Randomization analysis showed that projections based on the set of 82 genes led to significant correlations between the initial and barcode scRNA-seq levels (based on both rank-sum and t tests; Table S6). Using these genes for the projections, we found that only a few cells were assigned to the earlier paths (P0 and P1), whereas over 90% of cells were correctly assigned to the later paths (after P0 and P1). As for the two major branches (top, non-lung; bottom, lung), we found that 13/14 (92.9%) of the largest clones (>30 cells) were assigned to both paths and 108/272 of all clones (39.7%) with >1 cell were assigned to both top and bottom paths (Table S5). Projecting the largest clones (≥ 30 cells) on cell-fate paths predicted by CSHMM (Figures 6E and 6F) suggested that no predominant clone contributed uniquely to each cell-fate path confirming that cells may still switch cell fate after day 17.

While the two complementary analysis methods we used, tSNE cluster assignments (unsupervised) and CSHMM projections (supervised) led to the same conclusions about multipotency, we further examined the agreement of each method for each of the largest clones (>30 cells). We found overall good agreement between the way the largest clones were assigned by the two methods (Table S7). Taken together, these results indicate that DNA barcoding agrees with the CSHMM prediction that cell fate is not completely decided before day 17, and therefore PSC-derived progenitors are still “plastic” or multipotent at this developmental stage.

Time-Dependent Maturation Results in Stabilization of Lung Epithelial Cell Fates Allowing Indefinite Expansion of iAEC2s in Culture

Our detailed model covered the period between D15 and D31 and identified several branching events and their regulation with a specific path leading to the desired iAEC2 phenotype. We hypothesized that the frequency of reversion to non-lung endoderm, observed in the model, might decline over time as cells mature, allowing the propagation in culture of PSC-derived lung cells with more stable phenotypes (Figure 7A). To test for this possibility, we evaluated RUES2 ESCs, BU3 NGST iPSCs, as well as two additional iPSC lines (SPC2 and ABCA35), each targeted with our SFTPC^{tdTomato} reporter to allow real-time monitoring of distal lung fate. Differentiating each line via purified lung progenitors (sorted on day 15) again resulted in a day 30 cell population that contained mixed lung (NKX2-1⁺) and non-lung

(D) tSNE plots with Louvain clustering for annotated cell lineage and selected overlaid lentivirally barcoded clones. Clones X360, X8, and X232 are found contributing to multiple cell lineages (Multipotent), whereas others contribute only to lung lineage (X314), lung and PNEC (X401), and NLE only (X123).

(E) Lentivirally barcoded cells projected onto the CSHMM based using 86 selected genes. Clones are colored based on individual lentiviral barcodes, indicating clones arising from distinctly tagged individual ancestors.

(F) Bar charts showing the percentage of barcoded cells assigned to top and bottom paths. Similar proportions of cells are assigned to the paths as were seen in the original dataset (without lentiviral infection) indicating that the insertion of the virus did not appreciably impact or bias the differentiation of cells.

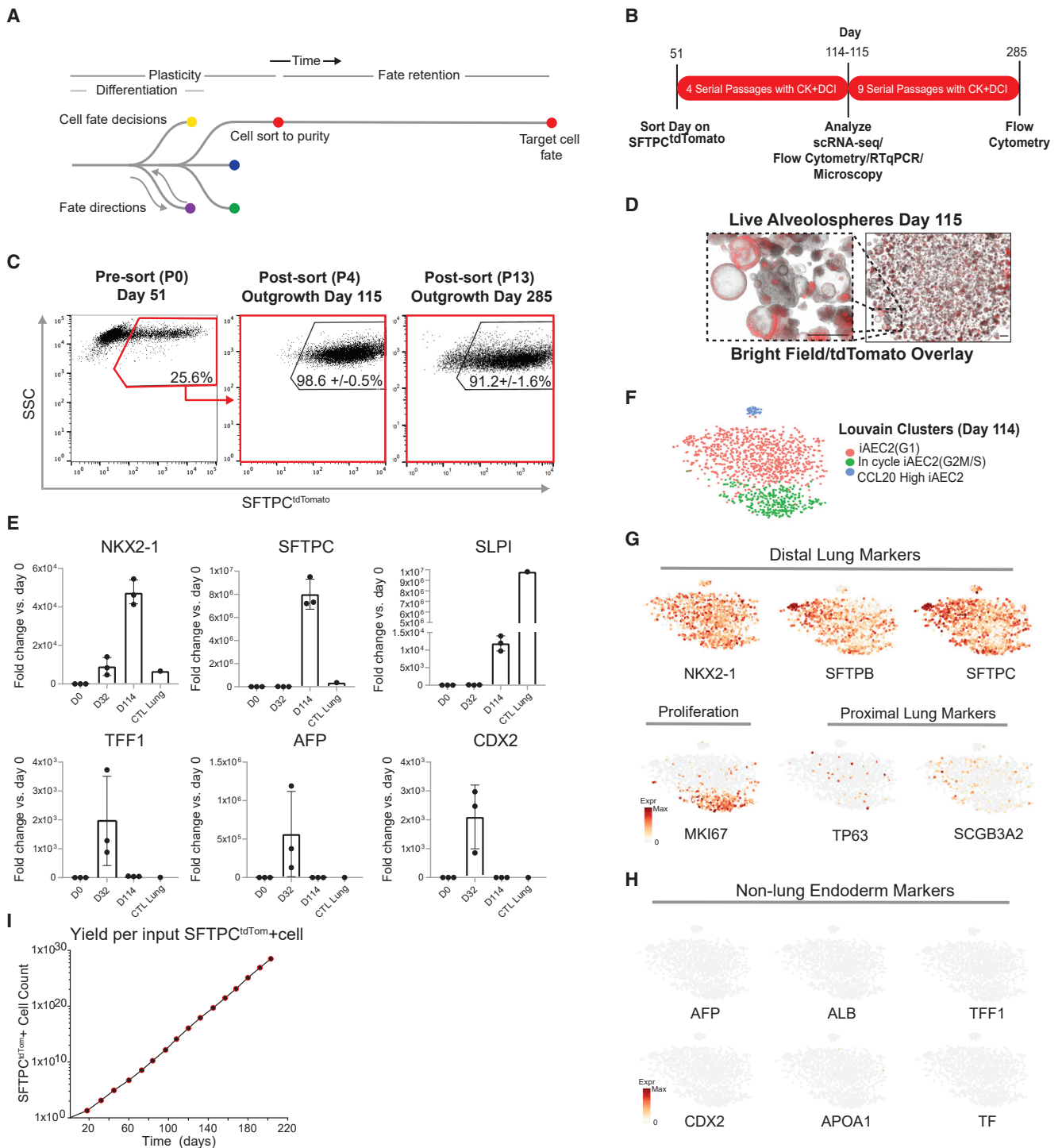


Figure 7. Time-Dependent Maturation Leads to Stabilized Lung Fate Retention of iAEC2

(A) Overview schematic of differentiation, maturation, and fate retention after mature cells are sorted to purity and further cultured for extended periods of time without loss of lung cell fate.

(B) Schematic of experiment in which cells sorted at day 51 for SFTPC^{tdTomato} were replated in 3D conditions in CK⁺DCI media and subsequently passaged as single cells 4 times on the days indicated, without further cell sorting. At days 114 and 115, cells were isolated for RT-qPCR, and live cells were encapsulated for scRNA-seq, respectively. Remaining cells were cultured for a further 170 days to day 285.

(C) Flow cytometry dot plots of cells before sorting for SFTPC^{tdTomato} and after replating tdTomato⁺ cells for outgrowth as alveolospheres. Repeated flow cytometry was performed after 4 passages (P4) on day 115 without additional sorting for scRNA-seq and repeated at each passage until day 285. Almost all cells have retained expression of the SFTPC lung reporter (mean ± SD is indicated; n = 3 biological replicates).

(legend continued on next page)

endoderm (NKX2-1-). However, resorting this population based on SFTPC^{tdTomato} expression after this period (day 51) (Figures 7B and 7C) resulted in the outgrowth of epithelial spheres that maintained SFTPC^{tdTomato} expression indefinitely, as we have previously published for RUES2 and BU3 cell lines (Jacob et al., 2017). We validated this same pattern for SPC2 and ABCA35 iPSCs, finding each line maintained SFTPC^{tdTomato} expression in >95% of cells followed as serially passaged cell cultures for at least 234 days and 102 days after sorting SFTPC^{tdTomato}⁺ cells on days 51 or 34 of differentiation, respectively (13 passages post-sorting; Figures 7C–7E and Figure S6; total differentiation time 285 and 136 days, respectively). scRNA-seq of the outgrowths from each line were prepared without further purification, and tSNE visualizations validated retention of distal lung phenotype in almost all cells without reversion to non-lung endoderm (Figures 7F–7H; Figure S6). For example, <0.1% of SPC2-derived cells at the day 115 time point expressed the gut marker CDX2 or hepatic markers TF, AFP, or ALB, and only 2 out of 1,390 cells expressed gastric marker TFF1 (Figure 7H). All cell clusters expressed high levels of NKX2-1 and AEC2 markers (Figure 7G) with similar findings in ABCA35 iPSC-derived cells (Figure S6). Based on this stability in iAEC2 phenotype, using this approach, we could generate 10³⁰ iAEC2s per input sorted tdTomato⁺ cell over a 225-day period without further cell sorting (Figure 7I). We did not observe evidence of reversion of non-lung lineages to either iAEC2s or NKX2-1⁺ lung epithelium in cells sorted on days 14–15 (Figure S7) in differentiation cultures, consistent with our previous findings in multiple human PSC lines (Hawkins et al., 2017; Jacob et al., 2017) and supporting the developmental concept of posterior (hindgut) dominance found during embryonic anterior-posterior patterning of the gut tube (Grapin-Botton, 2005). Taken together, these results suggested that, as in other *in vivo* developmental systems, there is a time-dependent loss of plasticity and stabilization or restriction of cell lineage in our model system.

DISCUSSION

To improve our understanding of PSC differentiation protocols, we developed a new framework that combines experimental design, computational modeling, lentiviral barcoding, and scRNA-seq profiling. As is evident by tracing descendants of lentivirally barcoded parents, clonal plasticity is observed in our PSC-derived system leading to lung and NLE cell fates, a finding that parallels *in vivo* observations where developing or adult lung epithelia tend to revert to NLE fates in abnormal or diseased settings where exuberant Wnt activity is present or where there is loss of Nkx2-1 (Herriges et al., 2014; Little et al., 2019; Okubo

and Hogan, 2004; Snyder et al., 2013; Tata et al., 2018). For example, Hogan and colleagues found non-lung endoderm, such as intestinal programs, emerged in mouse lung epithelial cells *in vivo* after lineage-specific conditional hyperactivation of canonical Wnt signaling (Okubo and Hogan, 2004). In addition, in settings where Nkx2-1 expression is lost, multiple lung epithelia revert to NLE fates in either fetal or adult lungs (Little et al., 2019) through a mechanism that involves loss of repression of Foxa2-driven non-lung fates (Snyder et al., 2013). This emergence of NLE descendants from lung epithelial parents is particularly evident in lung adenocarcinoma settings (Snyder et al., 2013; Tata et al., 2018), suggesting that our model may provide insights for understanding and preventing the fate changes that occur during lung cancer pathogenesis.

We validated the parent-progeny relationships predicted using a combination of scRNA-seq and lentiviral barcoding (Weinreb et al., 2020). Genetic tagging of individual cells allowed tracing of their progeny during directed differentiation. Such an approach can match lineage relationships in both a supervised and unsupervised manner, as has been recently reported (Biddu et al., 2018; Wagner et al., 2018). Finally, we also found that cells that are assigned to the AEC2 path in our model appear to stabilize their phenotypes, consistent with *in vivo* patterns of time-dependent restrictions of developing fates including endodermal lineages (Grapin-Botton, 2005). This leads to an expandable pool of lung progenitors that maintain stable AEC2-like fate even after extensive proliferation *in vitro*.

Our work provides insights into human lung development including further assessment of the role of early modulation of the Wnt pathway after initial human lung specification in specifying AEC2 fate and the identification of CEBP δ , previously known to play a role in mouse AEC2 differentiation, as a regulator of AEC2 differentiation in human development. In addition, our work identifies a period of fate plasticity occurring after lung specification, evident as retained endodermal multipotency, which subsides over time, allowing later cells to better maintain fate stability. Our results suggest mechanistic explanations for the widespread observation that PSC-directed differentiation results in heterogeneous lineages that are notoriously difficult to maintain in stable form in the presence of potent growth factors. More sophisticated modulation of growth factor dose responses with precise spatiotemporal control is likely to be required in future studies to properly stabilize and control cellular fate, purity, and maturation when deriving lung cells from PSCs for future regenerative medicine applications. The computational framework described here has multiple practical applications to the wider stem cell biology community and is accessible through open source code and web visualization engines detailed in

(D) Representative images of live SPC2 alveolospheres (bright-field/tdTomato overlay; day 115) illustrating retention of lung fate, indicated by continued expression of SFTPC^{tdTomato}. Scale bar, 500 μ m.

(E) Relative expression levels of each indicated AEC2 or endodermal marker transcript (RT-qPCR) in iAEC2s at day 0 (D0), at day 32 (D32) before sorting for a pure population of SFTPC^{tdTomato}, and at day 114 (D114; four passages after tdTomato⁺ sorting and extended culture.) Control samples are an adult human distal lung explant (CTL Lung).

(F) tSNE with Louvain clusters annotated using marker genes for iAEC2 in the G1 phase of cell cycle, markers of iAEC2s in the G2M/S cell-cycle stages “in cycle iAEC2(G2M/S)”, and markers of iAEC2 with high CCL20 expression.

(G and H) Normalized gene expression overlaid on tSNE plots for each indicated markers of (G) distal lung, proliferation, proximal lung, or (H) non-lung endoderm.

(I) Line graph of yield per input SFTPC^{tdTomato}⁺ cell. In a separate differentiation experiment, SPC2 cells were sorted for SFTPC^{tdTomato}⁺ cells at day 45, and the outgrowth was cultured for 15 passages (203 additional days). SFTPC^{tdTomato}⁺ positive yield at each passage (n = 3) is shown without further cell sorting.

the **STAR Methods**. Thus, our approach can be immediately applied for the analysis of scRNA-seq time series datasets, particularly those focused on differentiating stem cells. Unlike most prior methods for reconstruction of trajectories from scRNA-seq data, CSHMM uses a probabilistic model that utilizes all genes to infer cell assignments and branching, thereby overcoming noise and internal stochasticity, both hallmarks of stem cell data (Dong and Liu, 2017).

Several limitations to our methods are important to highlight. While we sampled cells at the earliest possible time after sorting for progenitors, earlier acquisition of endodermal samples before sorting on the lung progenitor marker NKX2-1 or the use of epigenetic profiling could identify pre-patterning of fates that might have been missed in our transcriptomic profiles. Second, our method was designed to detect multipotency and fate bifurcations rather than to quantify any lineage bias that may be present at each developmental stage. Others have published lentiviral barcoding over time that might be employed to more precisely quantify lineage bias at each stage in our protocol (Biddy et al., 2018; Weinreb et al., 2018a). It should be pointed out that prior time series profiles have revealed fate convergence from distinct origins is detectable in the development of alternate germ layer derivatives (e.g., neural crest cells; Wagner et al., 2018); however, we found only divergence to be present in our lung developmental trajectories, suggesting convergence may not contribute to the emergence of AEC2s. These results are consistent with prior observations that all distal lung epithelial descendants arise via the gateway of an endodermal NKX2-1⁺ progenitor, rather than from alternate origins (Hawkins et al., 2017; Jacob et al., 2017; Longmire et al., 2012).

Despite these limitations, the framework which we have developed, combining predictive computational approaches with cell-fate tracing is generalizable. It can be used to further understand and model several other directed differentiation strategies and disease pathogenesis, potentially leading to future cell therapies.

STAR★METHODS

Detailed methods are provided in the online version of this paper and include the following:

- **KEY RESOURCES TABLE**
- **LEAD CONTACT AND MATERIALS AVAILABILITY**
- **EXPERIMENTAL MODEL AND SUBJECT DETAILS**
 - Isolation of primary fetal and adult AECs
 - iPSC Line Generation and Maintenance
- **METHOD DETAILS**
 - Bulk RNA Sequencing
 - Directed Differentiation of PSCs
 - NanoString Time Series
 - Time Point Selection (TPS) Analysis
 - Time Series Single-Cell Transcriptomic Analysis of AEC2 Directed Differentiation
 - Predicting and mapping fate trajectories using Continuous State Hidden Markov Models (CSHMM)
 - CSHMM Prediction of Optimal Wnt Withdrawal Time and Confirmation by Direct Experiment
 - Lineage Tracing of PSC-derived iAEC2 Differentiation Using Lentiviral Barcoding

- Isolation of SFTPC^{tdTomato}-expressing iAEC2s and Long-Term Culture of Alveolospheres
- Determining Fate Retention in Additional iPSC lines
- **QUANTIFICATION AND STATISTICAL ANALYSIS**
 - Reverse Transcriptase Quantitative PCR
 - Statistical Methods
- **DATA AND CODE AVAILABILITY**
- **ADDITIONAL RESOURCES**

SUPPLEMENTAL INFORMATION

Supplemental Information can be found online at <https://doi.org/10.1016/j.stem.2019.12.009>.

ACKNOWLEDGMENTS

The authors wish to thank Caleb Weinreb and Allon Klein of Harvard Medical School for assistance with their lentiviral barcoding library, access to the HMS inDrops core facility, and application of SPRING software. We thank Yuriy Alekseyev of the Boston University School of Medicine (BUSM) Single Cell Sequencing Core and Brian R. Tilton of the BUSM Flow Cytometry Core, both supported by National Institutes of Health, United States grant 1UL1TR001430. For facilities management, we thank Greg Miller, CReM Laboratory Manager, and Marianne James, CReM iPSC Core Manager, supported by grants R24HL123828 and U01TR001810. We thank Michael Morley at the University of Pennsylvania for access to his bioinformatics portal for analyses of bulk RNA-seq datasets and Afric White for her constructive contribution to the work. The current work was supported by an Alpha-1 Foundation Postdoctoral Fellowship Award (K.H.), TL1TR001410 and F31HL134274 (A.J.), F30HL142169 (Y.L.S.), the I.M. Rosenzweig Junior Investigator Award from the Pulmonary Fibrosis Foundation (K.D.A.), R01GM122096 and R01HL128172 (Z.B.-J. and D.N.K.), OT2OD026682 (Z.B.-J.), and R01HL095993, R01HL122442, U01HL134745, and U01HL134766 (D.N.K.).

AUTHOR CONTRIBUTIONS

K.H., D.N.K., Z.B.-J., and J.D. designed the project, performed experiments and bioinformatic analysis, and wrote the manuscript. K.H., M.J.H., K.D.A., Y.L.S., R.B.W., A.M., A.J., and M.V. performed differentiation experiments, and K.H., M.J.H., K.D.A., and Y.L.S. performed scRNA-seq experiments. Z.B.-J., C.L. and J.D. developed CSHMM. C.V.-M. and I.S.C. analyzed scRNA-seq and RNA-seq experiments and performed statistical analysis. S.H.G. provided primary fetal lung samples, which were analyzed by A.J. by bulk RNA-seq. F.A., N.K., and I.O. performed NanoString mRNA quantification and analysis. A.R.-F and F.C. developed the barcoding lentivirus.

DECLARATION OF INTERESTS

Dr. Kaminski reports consultant fees from Biogen Idec, Boehringer Ingelheim, Third Rock, Pliant, Samumed, NuMedii, Indaloo, Theravance, LifeMax, and the Helmsley Foundation, non-financial support from Miragen, all outside the submitted work. In addition, Dr. Kaminski has patents on New Therapies in Pulmonary Fibrosis (licensed) and patents on peripheral blood biomarkers in IPF. The other authors declare no competing interests.

Received: May 26, 2019
Revised: November 4, 2019
Accepted: December 19, 2019
Published: January 30, 2020

REFERENCES

Biddy, B.A., Kong, W., Kamimoto, K., Guo, C., Wayne, S.E., Sun, T., and Morris, S.A. (2018). Single-cell mapping of lineage and identity in direct reprogramming. *Nature* 564, 219–224.

- Cao, J., Spielmann, M., Qiu, X., Huang, X., Ibrahim, D.M., Hill, A.J., Zhang, F., Mundlos, S., Christiansen, L., Steemers, F.J., et al. (2019). The single-cell transcriptional landscape of mammalian organogenesis. *Nature* **566**, 496–502.
- Desai, T.J., Brownfield, D.G., and Krasnow, M.A. (2014). Alveolar progenitor and stem cells in lung development, renewal and cancer. *Nature* **507**, 190–194.
- Ding, J., Aronow, B.J., Kaminski, N., Kitzmiller, J., Whitsett, J.A., and Bar-Joseph, Z. (2018). Reconstructing differentiation networks and their regulation from time series single-cell expression data. *Genome Res.* Published online January 9, 2018. <https://doi.org/10.1101/gr.252597.117>.
- Dobin, A., Davis, C.A., Schlesinger, F., Drenkow, J., Zaleski, C., Jha, S., Batut, P., Chaisson, M., and Gingeras, T.R. (2013). STAR: ultrafast universal RNA-seq aligner. *Bioinformatics* **29**, 15–21.
- Dong, P., and Liu, Z. (2017). Shaping development by stochasticity and dynamics in gene regulation. *Open Biol.* **7**, 7.
- Edgar, R., Domrachev, M., and Lash, A.E. (2002). Gene Expression Omnibus: NCBI gene expression and hybridization array data repository. *Nucleic Acids Res.* **30**, 207–210.
- Ernst, J., Vainas, O., Harbison, C.T., Simon, I., and Bar-Joseph, Z. (2007). Reconstructing dynamic regulatory maps. *Mol. Syst. Biol.* **3**, 74.
- Finak, G., McDavid, A., Yajima, M., Deng, J., Gersuk, V., Shalek, A.K., Slichter, C.K., Miller, H.W., McElrath, M.J., Prlic, M., et al. (2015). MAST: a flexible statistical framework for assessing transcriptional changes and characterizing heterogeneity in single-cell RNA sequencing data. *Genome Biol.* **16**, 278.
- Frank, D.B., Peng, T., Zepp, J.A., Snitow, M., Vincent, T.L., Penkala, I.J., Cui, Z., Herriges, M.J., Morley, M.P., Zhou, S., et al. (2016). Emergence of a Wave of Wnt Signaling that Regulates Lung Alveologenesis by Controlling Epithelial Self-Renewal and Differentiation. *Cell Rep.* **17**, 2312–2325.
- Gonzales, L.W., Guttentag, S.H., Wade, K.C., Postle, A.D., and Ballard, P.L. (2002). Differentiation of human pulmonary type II cells in vitro by glucocorticoid plus cAMP. *Am. J. Physiol. Lung Cell. Mol. Physiol.* **283**, L940–L951.
- Gotoh, S., Ito, I., Nagasaki, T., Yamamoto, Y., Konishi, S., Korogi, Y., Matsumoto, H., Muro, S., Hirai, T., Funato, M., et al. (2014). Generation of alveolar epithelial spheroids via isolated progenitor cells from human pluripotent stem cells. *Stem Cell Reports* **3**, 394–403.
- Grapin-Botton, A. (2005). Antero-posterior patterning of the vertebrate digestive tract: 40 years after Nicole Le Douarin's PhD thesis. *Int. J. Dev. Biol.* **49**, 335–347.
- Guo, M., Du, Y., Gokey, J.J., Ray, S., Bell, S.M., Adam, M., Sudha, P., Perl, A.K., Deshmukh, H., Potter, S.S., et al. (2019). Single cell RNA analysis identifies cellular heterogeneity and adaptive responses of the lung at birth. *Nat. Commun.* **10**, 37.
- Han, B., Chen, S.Y., Zhu, Y.T., and Tseng, S.C. (2014). Integration of BMP/Wnt signaling to control clonal growth of limb epithelial progenitor cells by niche cells. *Stem Cell Res. (Amst.)* **12**, 562–573.
- Hawkins, F., Kramer, P., Jacob, A., Driver, I., Thomas, D.C., McCauley, K.B., Skvir, N., Crane, A.M., Kurmann, A.A., Hollenberg, A.N., et al. (2017). Prospective isolation of NKX2-1-expressing human lung progenitors derived from pluripotent stem cells. *J. Clin. Invest.* **127**, 2277–2294.
- Herazo-Maya, J.D., Sun, J., Molyneaux, P.L., Li, Q., Villalba, J.A., Tzouveleki, A., Lynn, H., Juan-Guardela, B.M., Risquez, C., Osorio, J.C., et al. (2017). Validation of a 52-gene risk profile for outcome prediction in patients with idiopathic pulmonary fibrosis: an international, multicentre, cohort study. *Lancet Respir. Med.* **5**, 857–868.
- Herman, J.S., Sagar, and Grün, D. (2018). FateID infers cell fate bias in multipotent progenitors from single-cell RNA-seq data. *Nat. Methods* **15**, 379–386.
- Herriges, M.J., Swarr, D.T., Morley, M.P., Rath, K.S., Peng, T., Stewart, K.M., and Morrisey, E.E. (2014). Long noncoding RNAs are spatially correlated with transcription factors and regulate lung development. *Genes Dev.* **28**, 1363–1379.
- Hogan, B.L., Barkauskas, C.E., Chapman, H.A., Epstein, J.A., Jain, R., Hsia, C.C., Niklason, L., Calle, E., Le, A., Randell, S.H., et al. (2014). Repair and regeneration of the respiratory system: complexity, plasticity, and mechanisms of lung stem cell function. *Cell Stem Cell* **15**, 123–138.
- Holtzinger, A., Streeter, P.R., Sarangi, F., Hillborn, S., Niapour, M., Ogawa, S., and Keller, G. (2015). New markers for tracking endoderm induction and hepatocyte differentiation from human pluripotent stem cells. *Development* **142**, 4253–4265.
- Huang, S.X., Islam, M.N., O'Neill, J., Hu, Z., Yang, Y.G., Chen, Y.W., Mumau, M., Green, M.D., Vunjak-Novakovic, G., Bhattacharya, J., and Snoeck, H.W. (2014). Efficient generation of lung and airway epithelial cells from human pluripotent stem cells. *Nat. Biotechnol.* **32**, 84–91.
- Jacob, A., Morley, M., Hawkins, F., McCauley, K.B., Jean, J.C., Heins, H., Na, C.L., Weaver, T.E., Vedaie, M., Hurley, K., et al. (2017). Differentiation of Human Pluripotent Stem Cells into Functional Lung Alveolar Epithelial Cells. *Cell Stem Cell* **21**, 472–488.
- Jacob, A., Vedaie, M., Roberts, D.A., Thomas, D.C., Villacorta-Martin, C., Alysandratos, K.D., Hawkins, F., and Kotton, D.N. (2019). Derivation of self-renewing lung alveolar epithelial type II cells from human pluripotent stem cells. *Nat. Protoc.* **14**, 3303–3332.
- Zilionis, R., Nainys, J., Veres, A., Savova, V., Zemmour, D., Klein, A.M., and Mazutis, L. (2017). Single-cell barcoding and sequencing using droplet microfluidics. *Nat. Protoc.* **12**, 44–73.
- Klein, A.M., Mazutis, L., Akartuna, I., Tallapragada, N., Veres, A., Li, V., Peshkin, L., Weitz, D.A., and Kirschner, M.W. (2015). Droplet barcoding for single-cell transcriptomics applied to embryonic stem cells. *Cell* **161**, 1187–1201.
- Kleyman, M., Sefer, E., Nicola, T., Espinoza, C., Chhabra, D., Hagood, J.S., Kaminski, N., Ambalavanan, N., and Bar-Joseph, Z. (2017). Selecting the most appropriate time points to profile in high-throughput studies. *eLife* **6**. Published online January 26, 2017. <https://doi.org/10.7554/eLife.18541>.
- Kurmann, A.A., Serra, M., Hawkins, F., Rankin, S.A., Mori, M., Astapova, I., Ullas, S., Lin, S., Bilodeau, M., Rossant, J., et al. (2015). Regeneration of Thyroid Function by Transplantation of Differentiated Pluripotent Stem Cells. *Cell Stem Cell* **17**, 527–542.
- Law, C.W., Chen, Y., Shi, W., and Smyth, G.K. (2014). voom: Precision weights unlock linear model analysis tools for RNA-seq read counts. *Genome Biol* **15**, R29.
- Li, J.Z., Bunney, B.G., Meng, F., Hagenauer, M.H., Walsh, D.M., Vawter, M.P., Evans, S.J., Choudary, P.V., Cartagena, P., Barchas, J.D., et al. (2013). Circadian patterns of gene expression in the human brain and disruption in major depressive disorder. *Proc. Natl. Acad. Sci. USA* **110**, 9950–9955.
- Lin, C., and Bar-Joseph, Z. (2019). Continuous-state HMMs for modeling time-series single-cell RNA-Seq data. *Bioinformatics* **35**, 4707–4715.
- Little, D.R., Gerner-Mauro, K.N., Flodby, P., Crandall, E.D., Borok, Z., Akiyama, H., Kimura, S., Ostrin, E.J., and Chen, J. (2019). Transcriptional control of lung alveolar type 1 cell development and maintenance by NK homeobox 2-1. *Proc. Natl. Acad. Sci. USA* **116**, 20545–20555.
- Longmire, T.A., Ikononou, L., Hawkins, F., Christodoulou, C., Cao, Y., Jean, J.C., Kwok, L.W., Mou, H., Rajagopal, J., Shen, S.S., et al. (2012). Efficient derivation of purified lung and thyroid progenitors from embryonic stem cells. *Cell Stem Cell* **10**, 398–411.
- McCauley, K.B., Hawkins, F., Serra, M., Thomas, D.C., Jacob, A., and Kotton, D.N. (2017). Efficient Derivation of Functional Human Airway Epithelium from Pluripotent Stem Cells via Temporal Regulation of Wnt Signaling. *Cell Stem Cell* **20**, 844–857.
- McCauley, K.B., Alysandratos, K.D., Jacob, A., Hawkins, F., Caballero, I.S., Vedaie, M., Yang, W., Slovik, K.J., Morley, M., Carraro, G., et al. (2018). Single-Cell Transcriptomic Profiling of Pluripotent Stem Cell-Derived SCGB3A2⁺ Airway Epithelium. *Stem Cell Reports* **10**, 1579–1595.
- Miller, A.J., Hill, D.R., Nagy, M.S., Aoki, Y., Dye, B.R., Chin, A.M., Huang, S., Zhu, F., White, E.S., Lama, V., and Spence, J.R. (2018). In Vitro Induction and In Vivo Engraftment of Lung Bud Tip Progenitor Cells Derived from Human Pluripotent Stem Cells. *Stem Cell Reports* **10**, 101–119.
- Mithal, A., Capilla, A., Heinze, D., Berical, A., Villacorta-Martin, C., Vedaie, M., Jacob, A., Abo, K., Szymaniak, A., Peasley, M., et al. (2020). Generation of mesenchyme free intestinal organoids from human induced pluripotent stem cells. *Nat Commun* **11**, <https://doi.org/10.1038/s41467-019-13916-6>.

- Mucenski, M.L., Wert, S.E., Nation, J.M., Loudy, D.E., Huelsenken, J., Birchmeier, W., Morrisey, E.E., and Whitsett, J.A. (2003). beta-Catenin is required for specification of proximal/distal cell fate during lung morphogenesis. *J. Biol. Chem.* *278*, 40231–40238.
- Ng, R.C., Matsumaru, D., Ho, A.S., Garcia-Barceló, M.M., Yuan, Z.W., Smith, D., Kodjabachian, L., Tam, P.K., Yamada, G., and Lui, V.C. (2014). Dysregulation of Wnt inhibitory factor 1 (Wif1) expression resulted in aberrant Wnt- β -catenin signaling and cell death of the cloaca endoderm, and anorectal malformations. *Cell Death Differ.* *21*, 978–989.
- Nikolić, M.Z., Carigt, O., Jeng, Q., Johnson, J.A., Sun, D., Howell, K.J., Brady, J.L., Laresgoiti, U., Allen, G., Butler, R., et al. (2017). Human embryonic lung epithelial tips are multipotent progenitors that can be expanded in vitro as long-term self-renewing organoids. *eLife* *6*. Published online June 30, 2017. <https://doi.org/10.7554/eLife.26575>.
- Nikolić, M.Z., Sun, D., and Rawlins, E.L. (2018). Human lung development: recent progress and new challenges. *Development* *145*, 145.
- Okubo, T., and Hogan, B.L. (2004). Hyperactive Wnt signaling changes the developmental potential of embryonic lung endoderm. *J. Biol.* *3*, 11.
- Perl, A.K., Kist, R., Shan, Z., Scherer, G., and Whitsett, J.A. (2005). Normal lung development and function after Sox9 inactivation in the respiratory epithelium. *Genesis* *41*, 23–32.
- Plasschaert, L.W., Žilionis, R., Choo-Wing, R., Savova, V., Knehr, J., Roma, G., Klein, A.M., and Jaffe, A.B. (2018). A single-cell atlas of the airway epithelium reveals the CFTR-rich pulmonary ionocyte. *Nature* *560*, 377–381.
- Rashid, S., Kotton, D.N., and Bar-Joseph, Z. (2017). TASIC: determining branching models from time series single cell data. *Bioinformatics* *33*, 2504–2512.
- Rockich, B.E., Hrycaj, S.M., Shih, H.P., Nagy, M.S., Ferguson, M.A., Kopp, J.L., Sander, M., Wellik, D.M., and Spence, J.R. (2013). Sox9 plays multiple roles in the lung epithelium during branching morphogenesis. *Proc. Natl. Acad. Sci. USA* *110*, E4456–E4464.
- Schiebinger, G., Shu, J., Tabaka, M., Cleary, B., Subramanian, V., Solomon, A., Gould, J., Liu, S., Lin, S., Berube, P., et al. (2019). Optimal-Transport Analysis of Single-Cell Gene Expression Identifies Developmental Trajectories in Reprogramming. *Cell* *176*, 1517.
- Schwartzentruber, J., Foskolou, S., Kilpinen, H., Rodrigues, J., Alasoo, K., Knights, A.J., Patel, M., Goncalves, A., Ferreira, R., Benn, C.L., et al.; HIPSCI Consortium (2018). Molecular and functional variation in iPSC-derived sensory neurons. *Nat. Genet.* *50*, 54–61.
- Serra, M., Alysandratos, K.D., Hawkins, F., McCauley, K.B., Jacob, A., Choi, J., Caballero, I.S., Vedaie, M., Kurmann, A.A., Ikonomou, L., et al. (2017). Pluripotent stem cell differentiation reveals distinct developmental pathways regulating lung- versus thyroid-lineage specification. *Development* *144*, 3879–3893.
- Shu, W., Guttentag, S., Wang, Z., Andl, T., Ballard, P., Lu, M.M., Piccolo, S., Birchmeier, W., Whitsett, J.A., Millar, S.E., and Morrisey, E.E. (2005). Wnt/beta-catenin signaling acts upstream of N-myc, BMP4, and FGF signaling to regulate proximal-distal patterning in the lung. *Dev. Biol.* *283*, 226–239.
- Snyder, E.L., Watanabe, H., Magendantz, M., Hoersch, S., Chen, T.A., Wang, D.G., Crowley, D., Whittaker, C.A., Meyerson, M., Kimura, S., and Jacks, T. (2013). Nkx2-1 represses a latent gastric differentiation program in lung adenocarcinoma. *Mol. Cell* *50*, 185–199.
- Somers, A., Jean, J.C., Sommer, C.A., Omari, A., Ford, C.C., Mills, J.A., Ying, L., Sommer, A.G., Jean, J.M., Smith, B.W., et al. (2010). Generation of transgene-free lung disease-specific human induced pluripotent stem cells using a single excisable lentiviral stem cell cassette. *Stem Cells* *28*, 1728–1740.
- Tan, M., Gong, H., Zeng, Y., Tao, L., Wang, J., Jiang, J., Xu, D., Bao, E., Qiu, J., and Liu, Z. (2014). Downregulation of homeodomain-interacting protein kinase-2 contributes to bladder cancer metastasis by regulating Wnt signaling. *J. Cell. Biochem.* *115*, 1762–1767.
- Tata, P.R., Chow, R.D., Saladi, S.V., Tata, A., Konkimalla, A., Bara, A., Montoro, D., Hariri, L.P., Shih, A.R., Mino-Kenudson, M., et al. (2018). Developmental History Provides a Roadmap for the Emergence of Tumor Plasticity. *Dev. Cell* *44*, 679–693.
- Tirosh, I., Izar, B., Prakadan, S.M., Wadsworth, M.H., 2nd, Treacy, D., Trombetta, J.J., Rotem, A., Rodman, C., Lian, C., Murphy, G., et al. (2016). Dissecting the multicellular ecosystem of metastatic melanoma by single-cell RNA-seq. *Science* *352*, 189–196.
- Trapnell, C., Cacchiarelli, D., Grimsby, J., Pokharel, P., Li, S., Morse, M., Lennon, N.J., Livak, K.J., Mikkelsen, T.S., and Rinn, J.L. (2014). The dynamics and regulators of cell fate decisions are revealed by pseudotemporal ordering of single cells. *Nat. Biotechnol.* *32*, 381–386.
- Treutlein, B., Brownfield, D.G., Wu, A.R., Neff, N.F., Mantalas, G.L., Espinoza, F.H., Desai, T.J., Krasnow, M.A., and Quake, S.R. (2014). Reconstructing lineage hierarchies of the distal lung epithelium using single-cell RNA-seq. *Nature* *509*, 371–375.
- Wade, K.C., Guttentag, S.H., Gonzales, L.W., Maschhoff, K.L., Gonzales, J., Kolla, V., Singhal, S., and Ballard, P.L. (2006). Gene induction during differentiation of human pulmonary type II cells in vitro. *Am. J. Respir. Cell Mol. Biol.* *34*, 727–737.
- Wagner, D.E., Weinreb, C., Collins, Z.M., Briggs, J.A., Megason, S.G., and Klein, A.M. (2018). Single-cell mapping of gene expression landscapes and lineage in the zebrafish embryo. *Science* *360*, 981–987.
- Weinreb, C., Rodriguez-Fraticelli, A., Camargo, F., and Klein, A. M. (2020). Lineage tracing on transcriptional landscapes links state to fate during differentiation. *Science*. <https://doi.org/10.1126/science.aaw3381>.
- Weinreb, C., Wolock, S., and Klein, A.M. (2018a). SPRING: a kinetic interface for visualizing high dimensional single-cell expression data. *Bioinformatics* *34*, 1246–1248.
- Weinreb, C., Wolock, S., Tusi, B.K., Socolovsky, M., and Klein, A.M. (2018b). Fundamental limits on dynamic inference from single-cell snapshots. *Proc. Natl. Acad. Sci. USA* *115*, E2467–E2476.
- Wu, H., Uchimura, K., Donnelly, E.L., Kirita, Y., Morris, S.A., and Humphreys, B.D. (2018). Comparative Analysis and Refinement of Human PSC-Derived Kidney Organoid Differentiation with Single-Cell Transcriptomics. *Cell Stem Cell* *23*, 869–881.
- Zarkou, V., Galaras, A., Giakountis, A., and Hatzis, P. (2018). Crosstalk mechanisms between the WNT signaling pathway and long non-coding RNAs. *Noncoding RNA Res.* *3*, 42–53.
- Nickles D, Sandmann T, Ziman R, Bourgon R (2018). NanoStringQCPro: Quality metrics and data processing methods for NanoString mRNA gene expression data. R package version 1.14.0.

STAR★METHODS

KEY RESOURCES TABLE

REAGENT or RESOURCE	SOURCE	IDENTIFIER
Antibodies		
Mouse monoclonal to CD26, PE conjugated (clone BA5b)	Biolegend	Cat#302705
Mouse monoclonal to CD47, PerCP-Cy5.5 conjugated (clone CC2C6)	Biolegend	Cat#323110
Chicken anti-GFP, unconjugated	Invitrogen	Cat#A10262
Rabbit anti-TTF1, unconjugated	Abcam	Cat#ab76013
Rabbit anti-CDX2, unconjugated	Invitrogen	Cat#MA5-14494
Donkey anti-chicken, Alexa Fluor 488-conjugated	Jackson ImmunoResearch	Cat#703-545-155
Goat anti-rabbit, Texas Red-conjugated	Abcam	Cat#ab6719
Hoechst 33342	Life Technologies	Cat#H3570
ProLong Diamond Antifade Mountant	Invitrogen	Cat#P36965
Cavity slides	Eisco	Cat#BI0086A
Chemicals, Peptides, and Recombinant Proteins		
Growth Factor Reduced Matrigel	Corning	Cat#356230
SB431542	Tocris	Cat#1614
Dorsomorphin	Stemgent	Cat#04-0024
CHIR99021	Tocris	Cat#4423
Recombinant human FGF10	R&D Systems	Cat#345-FG-025
Recombinant human KGF	R&D Systems	Cat#251-KG-010
Recombinant human BMP4	R&D Systems	Cat#314-BP
Retinoic acid	Sigma	Cat#R2625
Y-27632 dihydrochloride	Tocris	Cat#1254
Dexamethasone	Sigma	Cat#D4902
8-bromoadenosine 30,50-cyclic monophosphate sodium salt (cAMP)	Sigma	Cat#B7880
3-Isobutyl-1-methylxanthine (IBMX)	Sigma	Cat#I5879
0.05% trypsin-EDTA	Invitrogen	Cat#25300-120
Defined Fetal Bovine Serum	Thermo Fisher	Cat#NC0652331
Calcein blue	Life Technologies	Cat#C1429
Dispase	Thermo Fisher	Cat#354235
Critical Commercial Assays		
RNeasy Mini Kit	QIAGEN	Cat#74104
QIAzol Lysis Reagent QIAGEN	QIAGEN	Cat#79306
TaqMan Fast Universal PCR Master Mix (2X)	Thermo Fisher	Cat#4364103
High-Capacity cDNA Reverse Transcription Kit	Applied Biosystems	Cat#4368814
Lipfectamine LTX Kit	Thermo Fisher	Cat#15338100
Deposited Data		
Bulk RNA-seq series	This paper	GEO (GSE131768)
scRNA-seq time series This paper	This paper	GEO (GSE137811)
Lentiviral barcoding and lineage tracing	This paper	GEO (GSE137805)
Long-term culture of alveolospheres	This paper	GEO (GSE137799)
Experimental Models: Cell Lines		
Human: Normal donor iPSC line targeted with NKX2-1 ^{GFP} SFTPC ^{tdTomato} (BU3 NGST)	Kotton Lab (Jacob et al., 2017)	http://www.bu.edu/dbin/stemcells/
Human: Donor iPSC line targeted with SFTPC ^{tdTomato} (SPC2)	Kotton Lab	http://www.bu.edu/dbin/stemcells/

(Continued on next page)

Continued

REAGENT or RESOURCE	SOURCE	IDENTIFIER
Human: Donor iPSC line targeted with SFTPC ^{tdTomato} (ABCA35)	Kotton Lab	http://www.bu.edu/dbin/stemcells/
Human: RUES2 ST embryonic stem cell line targeted with SFTPC ^{tdTomato}	Original line is a gift from Dr. Ali H. Brivanlou, Rockefeller University; modified to include SFTPC ^{tdTomato} by the Kotton Lab in Jacob et al., 2017	http://www.bu.edu/dbin/stemcells/
Oligonucleotides		
TaqMan Gene Expression Assay Primer/Probe Sets	Thermo Fisher	
ABCA3	Thermo Fisher	Hs00975530_m1
AXIN2	Thermo Fisher	Hs00610344_m1
CEBPδ	Thermo Fisher	Hs00270931_s1
FOXA2	Thermo Fisher	Hs00232764_m1
LEF1	Thermo Fisher	Hs01547250_m1
NKX2-1	Thermo Fisher	Hs00968940_m1
SFTPA1	Thermo Fisher	Hs00831305_s1
SFTPC	Thermo Fisher	Hs00161628_m1
SFTPB	Thermo Fisher	Hs01090667_m1
Software and Algorithms		
ImageJ	National Institutes of Health	https://imagej.nih.gov/ij/
Continuous State Hidden Markov Model (CSHMM)	This paper and (Lin and Bar-Joseph, 2019)	http://cosimo.junding.me
Other		
StemDiff Definitive Endoderm Kit	StemCell Technologies	Cat#05110
mTeSR1	StemCell Technologies	Cat#05850
Glutamax	Life Technologies	Cat#35050-061
Gentle Cell Dissociation Reagent	StemCell Technologies	Cat#07174

LEAD CONTACT AND MATERIALS AVAILABILITY

All unique/stable reagents generated in this study are available from the Lead Contact with a completed Materials Transfer Agreement. Pluripotent stem cell lines generated in this study are available from the CREM Biobank at Boston University and Boston Medical Center and can be found at <http://www.bu.edu/dbin/stemcells/>. Further information and requests for other reagents may be directed to, and will be fulfilled by, the Lead Contact, Darrell Kotton (dkotton@bu.edu).

EXPERIMENTAL MODEL AND SUBJECT DETAILS

Isolation of primary fetal and adult AECs

Primary fetal lung alveolar epithelial cells and adult AEC2s were isolated for RNA extraction and analysis by bulk RNA-seq as detailed in our prior publication ([Jacob et al., 2017](#)) with partial datasets (for only the 21 week and adult cells) previously published in that manuscript and now re-deposited with the Gene Expression Omnibus (GEO) under GSE131768. For the present study 3 additional unpublished fetal alveolar epithelial samples from weeks 16-17.5 of gestation and 1 additional sample from week 20 of gestation was added for analysis. In order to avoid technical batch effects, all 13 samples for bulk RNA sequencing (day 15 PSC-derived primordial progenitors; n = 3 biological replicates; week 16-17.5 alveolar epithelium ; n = 3; week 20-21 alveolar epithelium; n = 4, and adult AEC2s; n = 3 donor lungs) underwent simultaneous parallel extraction of RNA, library preparation, and RNA sequencing. In brief each sample was isolated as follows: fetal lung tissue (weeks 16-21) was obtained in the Guttentag laboratory under protocols originally reviewed by the Institutional Review Board at the Children’s Hospital of Philadelphia and subsequently reviewed by Vanderbilt University. The cell stocks used in the present studies were donated to the Kotton laboratory for the purpose of providing reference data. Samples were isolated by the overnight culture of lung explants in Waymouth media; a technique that generally yields 86 ± 2% epithelial cells with the remaining cells consisting of fibroblasts with < 1% endothelial cells.

To isolate human primary lung epithelial cells, 1x1cm pieces of distal human lung obtained from healthy regions of the upper lobe of non-utilized human lungs donated for transplantation were dissected and all airway tissue and pleura was resected. Tissue was digested using dispase, collagenase I, and DNase using the gentle MACS 63 dissociator (Miltenyi) for 30 minutes at 37°C. The cell suspension was passed over 70µm and 40µm filters to generate a single cell suspension. Magnetic bead sorting using MACS

LS columns (Miltenyi) and the following antibodies: HTII-280 (anti-human AEC2 antibody, IgM, Terrace Biotechnologies) and anti-IgM magnetic beads (Miltenyi) was used to obtain purified human AEC2 cells and were subsequently collected into trizol.

iPSC Line Generation and Maintenance

All experiments involving the differentiation of human PSC lines were performed with the approval of the Institutional Review Board of Boston University (protocol H33122). The BU3 iPSC line carrying NKX2-1^{GFP} and SFTPC^{tdTomato} reporters (BU3 NGST) was obtained from our prior studies (Hawkins et al., 2017; Jacob et al., 2017). This line was derived from a normal donor (BU3) Kurmann et al., 2015). All PSC lines used in this study (BU3, RUES2, SPC2, and ABCA35) displayed a normal karyotype (BU3, 46XY; RUES2, 46XX; SPC2 46XY; and ABCA35 46XX) when analyzed by G-banding both before and after gene-editing (Cell Line Genetics). The human embryonic stem cell line RUES2 was a generous gift from Dr. Ali H. Brivanlou of The Rockefeller University. All PSC lines were maintained in feeder-free conditions, on growth factor reduced Matrigel (Corning) in 6-well tissue culture dishes (Corning), in mTeSR1 medium (StemCell Technologies) using gentle cell dissociation reagent for passaging. Further details of iPSC derivation, characterization, and culture are available for free download at <http://www.bu.edu/dbin/stemcells/protocols.php>.

METHOD DETAILS

Bulk RNA Sequencing

Sequencing libraries were prepared from the total RNA extracts of the above 13 samples using Illumina TruSeq RNA Sample Preparation Kit v2. The mRNA was isolated using magnetic beads-based poly(A) selection, fragmented, and randomly primed for reverse transcription, followed by second-strand synthesis to create double-stranded cDNA fragments. These cDNA fragments were then end-repaired, added with a single 'A' base, and ligated to Illumina® 64 Paired-End sequencing adapters. The products were purified and PCR-amplified to create the final cDNA library. The libraries from individual samples were pooled in groups of four for cluster generation on the Illumina cBot using Illumina TruSeq Paired-End Cluster Kit. Each group of samples was sequenced on each lane on the Illumina HiSeq 2500 to generate more than 30 million single end 100-bp reads.

Fastq files were assessed for quality control using the FastQC program. Fastq files were aligned against the human reference genome (hg19/hGRC37) using the STAR aligner (Dobin et al., 2013). Duplicate reads were flagged using the MarkDuplicates program from Picard tools. Gene counts represented as counts per million (CPM) were computed for Ensembl (v67) gene annotations using the Rsubread R package with duplicate reads removed. Genes with 10% of samples having a CPM < 1 were removed and deemed low expressed. The resultant data was transformed using the VOOM method implemented in limma R package (Law et al., 2014). Voom transformed data was then tested for differential gene expression using standard linear models using the limma package. Multiple hypothesis test correction was performed using the Benjamini–Hochberg procedure (FDR). Heatmaps and PCA plots were generated in R. All raw fastq files are available on-line at GEO (GSE13176).

Directed Differentiation of PSCs

As previously described (Jacob et al., 2017) we performed PSC directed differentiation via definitive endoderm into NKX2-1 lung progenitors as follows. In short, cells maintained on mTeSR1 media were differentiated into definitive endoderm using the STEMdiff Definitive Endoderm Kit (StemCell Technologies) and after the endoderm-induction stage, cells were dissociated with gentle cell dissociation reagent (GCDR) and passaged into 6 well plates pre-coated with growth factor reduced Matrigel in “DS/SB” anteriorization media, consisting of complete serum-free differentiation medium (cSFDM) base as previously described (Jacob et al., 2017) supplemented with 10 μ M SB431542 (“SB”; Tocris) and 2 μ M Dorsomorphin (“DS”; Stemgent). For the first 24 hr after passaging, 10 μ M Y-27632 was added to the media. After anteriorization in DS/SB media for 3 days (72 hr), cells were cultured in “CBRa” lung progenitor-induction media for 9–11 days. “CBRa” media consists of cSFDM containing 3 μ M CHIR99021 (Tocris), 10 ng/mL recombinant human BMP4 (rhBMP4, R&D Systems), and 100nM retinoic acid (RA, Sigma), as previously described (Jacob et al., 2017). On day 15 of differentiation, live cells were sorted on a high-speed cell sorted (MoFlo Legacy or MoFlo Astrios EQ) based on GFP expression for further differentiation or analysis as indicated in the text.

Sorted day 15 or 17 cells (as described in the text) were resuspended in undiluted growth factor-reduced Matrigel (Corning) at a dilution of 500 cells/ μ L, with droplets ranging in size from 25 to 100 μ L in 12 well tissue culture-treated plates (Corning). Cells in 3D Matrigel suspension were incubated at 37°C for 20–30 min, then warm media was added to the plates. Where indicated in the text, outgrowth and distal/alveolar differentiation of cells after day 15 was performed in “CK+DCI+Y” medium, consisting of cSFDM base, with 3 μ M CHIR99021, 10 ng/mL rhKGF, and 50 nM dexamethasone (Sigma), 0.1mM8-Bromoadenosine 30,50-cyclic monophosphate sodium salt (Sigma) and 0.1mM3-Isobutyl-1-methylxanthine (IBMX; Sigma) (DCI) and 10 μ M Y-27632. For NanoString mRNA analysis, alveolospheres were released from Matrigel droplets, and for flow cytometry and cell sorting, they were dissociated into single cell suspension. To release alveolospheres from Matrigel, droplets were incubated in dispase (2mg/ml, Fisher) at 37°C for 1 hr, centrifuged at 300 g x 1 min, washed in 1x PBS, then centrifuged again at 300 g x 1 min. To generate single cell suspensions, cell pellets were incubated in 0.05% trypsin and continued through the trypsin-based dissociation protocol described above, after which they could be passaged into fresh Matrigel and analyzed by flow cytometry.

NanoString Time Series

We used NanoString nCounter for direct quantification of 66 genes in triplicate of PSC differentiations based on a high-frequency sampling design: day 0, 17, 19, 21, 23, 25, 27, 29, 31, 33 with $n = 3$ late human fetal lung alveolar epithelial cell samples included as controls (Late HFL; 21 weeks gestation). RNA extraction was performed by miRNeasy MicroKit (QIAGEN) following the manufacturer's protocol. RNA concentration and integrity were measured using NanoDrop ND-2000 and 2200 Tape Station. The NanoString nCounter XT CodeSet Gene Expression Assay was performed using 100 ng total RNA as previously described (Herazo-Maya et al., 2017). The raw data was background corrected and normalized using NanoStringQCPro (Nickles et al., 2018). The estimation of non-specific noise for background correction was done using the signals obtained from negative controls in each lane. For content normalization we scaled each probe relative to the average signal from pre-annotated housekeeping genes. The average and range of the normalized values are shown in Figure 2 and Figure S1.

Time Point Selection (TPS) Analysis

We used the Time Points Selection (TPS) method (Kleyman et al., 2017) to determine time points to profile for accurate model reconstruction. Briefly, TPS utilizes NanoString nCounter quantification to obtain a densely sampled subset of genes which are known to be relevant to the process (in this case, known lung development genes; see Figures 2 and supplement). It then uses a greedy algorithm to identify the best time points to use given a limited budget (i.e., if the user can only profile x number of time points). TPS can also estimate the resulting error from using less time points and so provides a way to balance accuracy and costs. Here we searched for different values of x ranging from 4 to 8. As Figure 2 shows, we observe an elbow in the error plot when using 6 time points. Such elbow means that further increase in the number of time points does not lead to much decrease in error. For 6 time points the expected error (0.21, log₂ difference) is not far from the expected error due to repeats (0.16) which is the optimal error we can obtain and likely reflects real biological variations or technical issues. We thus used the 6 selected time points (15, 17, 21, 25, 29 and 31) to profile the single cells.

Time Series Single-Cell Transcriptomic Analysis of AEC2 Directed Differentiation

Time series cell capture and profiling by scRNA-seq with SPRING plot visualization

Day 15 BU NGST cells were sorted for NKX2-1^{GFP} (as described above) and live positive and negative sorted cells were acquired for scRNA-seq in the Harvard Medical School (HMS) scRNA-seq core laboratory. NKX2-1^{GFP} positive cells were replated in 3D matrigel and grown for a further 16 days to day 35. At the selected time points (days 15, 17, 21, 25, 29 and 31) cells derived from directed differentiation of the BU3 NGST iPSC line were stained with calcein blue viability dye and sorted to obtain live cells for scRNA-seq as detailed in the text. Cells were captured in the Harvard Medical School (HMS) Single Cell Core for scRNA-seq using inDrops technology, as follows. First cells were assessed for cell number and viability and resuspended in 1000 μ L of 15% OptiPrep to allow for a homogeneous resuspension and reduced clumping. Cell capture and library preparation were performed using a modified version of inDrops protocols (Klein et al., 2015; Plasschaert et al., 2018) involving encapsulation of cells into 3 nL droplets with hydrogel beads carrying barcoding reverse transcription primers. Following the within-droplet reverse transcription step, emulsions were split into batches of approximately 2,000 cells, frozen at -80°C , and subsequently processed as individual RNA-seq libraries. Approximately 4,000 cells for each time point were encapsulated for scRNA-seq.

The standard transcriptome RNA-seq libraries were processed as previously reported (Zilionis et al., 2017). In brief, the single cell libraries were demultiplexed following the recommended inDrops pipeline (<https://github.com/indrops/indrops>) in order to generate count matrices for each sample. We used the repeat-masked primary assembly of the human genome GRCh38 (ENSEMBL) as a reference. Reads were filtered according to the protocol to remove those that had low quality or low complexity. After counting and sorting abundant barcodes, histograms were used to identify thresholds that separate cells from empty gel beads. Finally, the reads of each barcode were aligned to the reference genome with Bowtie. Next, demultiplexed count matrices of the four libraries were aggregated into one combined analysis for downstream analysis. After further filtering to remove putative doublets as well as stressed or dying cells (having $> 20\%$ or UMIs coming from mitochondrial genes), we performed linear dimensionality reduction with PCA, which was then used as input for Louvain clustering and non-linear dimensionality reduction with tSNE. Cell cycle stage was scored and classified using the strategy described in (Tirosh et al., 2016). Differential expression was tested using hurdle models for sparse single-cell expression data implemented in MAST (Finak et al., 2015). The derived markers were used to annotate the identity of each cluster. Clonal identity was derived from the lineage barcoding spiked samples. The association between cellular barcodes and lentiviral barcodes from the spiked samples was connected to the transcriptomic samples for visualization. Lineage-annotated transcriptome data was then imported into SPRING (Weinreb et al., 2018a) for interactive analysis and visualization. All SPRING plots (k-NN graphs rendered using a force-directed layout) were generated in the SPRING upload server: <https://kleintools.hms.harvard.edu/tools/spring.html> using the default parameters: 0 minimum UMI total for filtering cells, minimum of 3 cells with ≥ 3 counts for filtering genes, 80 percentile as threshold of gene variability for filtering genes, 50 PCA dimensions for building graph, and a k of 5 for the k-Nearest Neighbors algorithm used to create the graph. Annotation tracks (clusters) were imported from upstream analysis with the Seurat package (Louvain algorithm at resolution 0.6) and gene sets for predicting the degree of maturation (6 gene set) and differentiation (8 gene set) were derived from the bulk RNA-seq data analysis (see Figure 1). The final figures were plotted using ggplot2 package (R-CRAN) and edges between nodes omitted for clarity. Datasets are available for download from GEO (GSE137811).

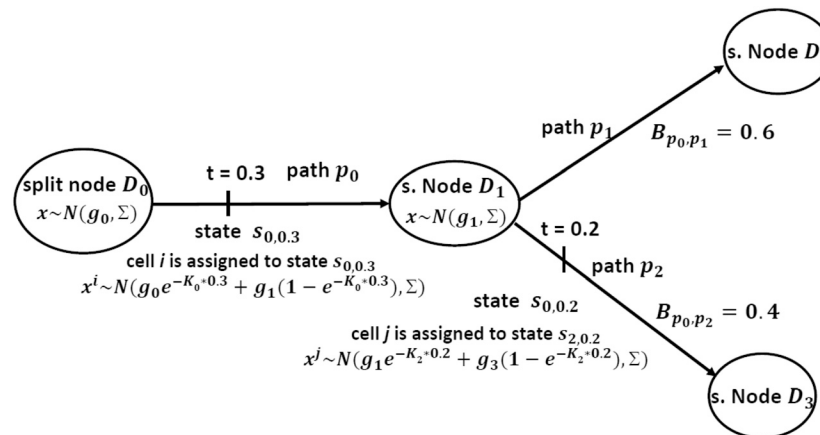
Predicting and mapping fate trajectories using Continuous State Hidden Markov Models (CSHMM)

We used Continuous State Hidden Markov Models (Lin and Bar-Joseph (2019)) to reconstruct the branching process of the data. The model was first initialized by clustering cells at each time point. Next, the location of each cluster was adjusted based on the distance to the root cluster (D15) to account for asynchronous development among cells at the same time point. In our case this led to placing cells from Day 21 and 25 at the same level of the branching tree because most overlapped in terms of expression (See also Spring plot in Figure 3 and Figure S2). For similar reasons we grouped cells at D29 and D31 at the same level. After assigning initial level, clusters in each level were connected to the nearest cluster in the previous level where distance is based on expression similarity leading to a tree-like branching structure. Finally, for the initializations, cells in each cluster were randomly placed on the paths connecting their node to their parent node (Figure 4A).

Next, CSHMM learned parameter values and cell assignments using an Expectation Maximization (EM) algorithm. In our CSHMM setting, neighboring states along a path share parameters and so, while the total number of states is potentially infinite the number of model parameters is still finite. The model is further constrained by allowing transition to only a finite (though not necessarily small) number of states from each state as shown in Schematic below. Parameters (learned in the M step) include standard HMM parameters as were used in previous bulk modeling methods (Ernst et al., 2007) and a new, gene specific parameter vector denoted by K_x (where x is the path number) which allows genes to change differently along a path. The structure and cell assignments also provide emission probabilities for each state. This enables the method to assign gene specific expression profiles for each of the paths while cell assignments, determined in the E step, are continuous and so cells can be assigned to any point along the path. Given the constraints on several aspects of the model, learning and inference is still efficient despite the infinite many possible states in a CSHMM. We stop when the likelihood of the model does not increase (Figure 4A). See Lin and Bar-Joseph (2019) for complete details.

Schematic: CSHMM model structure and parameters

Each path represents a set of infinite states parameterized by the path number and the location along the path. For each such state we define an emission probability and a transition probability to all other states in the model. Emission probability for a cell along a path is a function of the location of the state and a gene specific parameter for each gene in the cell which controls the rate of change of its expression along the path. Split nodes are locations where paths split and are associated with a branch probability. Each cell is assigned to a state in the model. As can be seen in Figure 4B (and in the interactive visualization) cells are not placed on the 'path line'



itself. Rather, cells are placed above or below the line with the distance indicating how well the expression for the state they are assigned to captures their expression. In other words, large distance from the line (either up or down depending on the number of over or under expressed genes) can be used to observe an earlier split by noticing that cells start to move away from the line at a certain point (for example, P7 cells are fairly noisy and not as well represented by the model as P1 cells and as a result are further from the line). Further details are available in: (Lin and Bar-Joseph, 2019).

CSHMM Prediction of Optimal Wnt Withdrawal Time and Confirmation by Direct Experiment

Determining time of split between cell fates

We used CSHMM assignments to infer the most appropriate time to withdraw Wnt. For this we selected a number of Wnt markers detailed in the text and plotted their continuous expression along the top and bottom paths (Figure 5). We used these plots to determine an accurate split time, in the model, for these markers. To determine the actual time the model point corresponds to the trajectory split, we assigned each N node in the CSHMM a real time which is computed by averaging the time in which cells assigned right before and right after the node were profiled (Figure 5B). Using these values, we assigned time to each point along a path by interpolating the time assigned to the two N nodes that define the path. For example, the split point identified for WNT is in the middle of the N1-N2 path. Since N1 is assigned to day 16 and D2 to day 19, this point is assigned to day 17.5.

Direct Wnt Withdrawal During NKX2-1+ Outgrowth Differentiation

Day 15 BU NGST cells were sorted for NKX2-1^{GFP} (as described above) and live positive sorted cells were replated in 3D Matrigel and grown for a further 14 days to day 29. We withdrew the GSK antagonist, CHIR from our “CK+DCI” media for a period of 4 days, starting at five different time points (days 17, 19, 21, 23 and 25; [Figure 5C](#)). To maintain proliferation of resulting cells CHIR was added back after 4 days, allowing each parallel condition to be harvested at the identical total differentiation time while keeping the length of CHIR withdrawal (4 days) constant for each condition. At day 29 a single cell suspension of all alveolospheres was generated and cells were analyzed by flow cytometry for NKX2-1^{GFP} and SFTPC^{tdTomato} reporter expression.

Knockdown of CEBP δ by siRNA transfection

The iPSC line, SPC2 was differentiated to alveolospheres as described above. Spheres were dissociated to single cells with trypsin, washed and counted. Cells (5×10^5 cells per reaction) were resuspended in a 20 μ L nucleofection reaction, as per manufacturer’s instructions (Lonza) (16.4 μ L P3 solution with 3.6 μ L supplement), with 500 nM of non-targeting siRNA (Dharmacon, #D-001810-01-05) or CEBP δ siRNA (Dharmacon, #L-010453-00-0005). Cells were transferred to a cuvette and nucleofected with program EA104 (4D Nucleofector; Lonza). Each reaction was replated in 100 μ L 3D Matrigel in CK+DCI+Y. Cells were collected, by dissolving Matrigel with dispase, at 48 hours for RNA isolation. CEBP δ (Hs00270931_s1), SFTPC (Hs00161628_m1), SFTPB (Hs00167036_m1), ABCA3 (Hs00184543_m1), SFTPA1 (Hs01652580_g1), NKX2-1 (Hs00968940_m1) and FOXA2 (Hs00232764_m1) transcripts were quantified by qRT-PCR and fold-change was calculated with respect to the non-targeting siRNA group as described in the section below.

Lineage Tracing of PSC-derived iAEC2 Differentiation Using Lentiviral Barcoding

Lentiviral barcoding

Lineage tracing of individual cells was performed using a lentiviral barcode labeling system ([Weinreb et al., 2020](#)). Human BU3 NGST cells were differentiated, sorted on D15 for NKX2-1^{GFP} positive cells and grown as alveolospheres, as described above, until D17. On D17 the Matrigel matrix was dissociated using 2mg/ml Dispase solution (ThermoFisher, 17105041) and 6.5×10^4 cells were resuspended in 600 μ L CK+DCI+RI with polybrene (5 μ g/ml). This cell suspension was divided equally into two suspensions: an uninfected control (MOI = 0) and a sample containing 32,500 cells which was infected with lentivirus (MOI = 10). Both samples were left in suspension for 4 hours before being washed and replated. Each sample was resuspended as cell clumps in 50 μ L Matrigel (Corning 356231) and plated as two 25 μ L droplets in one well of a 12-well plate previously coated with 100 μ L of Matrigel (Corning 356231). Cells were fed with CK+DCI+RI every 2 days until collection on D27, at which point cells were collected for single cell RNA-sequencing. Cells were collected using a MoFlo Astrios EQ cell sorter and enriched using calcein blue, to sort out live cells, and/or viral GFP expression.

Cell capture and library preparation were performed as described using a modified version of inDrops protocols ([Klein et al., 2015](#); [Plasschaert et al., 2018](#)). Prior to library preparation, RNA fractions generated from each population were split in half, with one half being used for standard library prep and the other half for targeted lineage barcode enrichment. To enrich for lineage barcodes, library preparation was modified as previously described ([Weinreb et al., 2020](#)) by skipping RNA fragmentation, priming the RT reaction using a barcode-specific primer (TGAGCAAAGACCCCAACGAG), introducing an extra PCR step using a targeted primer (8 cycles using Phusion 2X master mix; ThermoFisher; primer sequence = TCG TCG GCA GCG TCA GAT GTG TAT AAG AGA CAG NNN Ntaa ccg ttg cta gga gag acc atat), and 1.2X bead purification (Agencourt AMPure XP). All targeted and non-targeted final libraries were pooled at equimolar ratios and sequenced using Illumina NextSeq 500 Sequencing (75 Cycles, 75bp Single Read sequencing).

The lentivirus-targeted single-cell libraries were demultiplexed in the same way as the transcriptome libraries and further processed following the LARRY pipeline (Lineage And RNA RecoverY) described in ([Weinreb et al., 2020](#)). Briefly, this involves two steps: the first step was sorting and filtering the raw sequencing reads generated from the inDrops pipeline (<https://github.com/indrops/indrops>) which provides a list of reads with annotated cell barcode and unique molecular identifier (UMI); we used, as a threshold for collapsing lentivirus-barcode, a hamming distance of 3, and filtered out cell-lineage combinations that were not supported by at least 10 reads. The second step was annotating the clonality of cells, with further stringent filtering to discard contaminated droplets, which resulted in a NxM binary matrix of 0/1, where N is number of cells and M is the number of clones. The pipeline was executed using the implementation developed by Klein Lab, available online at: <https://github.com/AllonKleinLab/LARRY>. Datasets are available for download from GEO (GSE137805).

Projection of Barcoded Cells on CSHMM

Given experimental differences in profiling cells used to construct the model and barcoded cells we compared bar-coded cell expression values using a subset of 82 genes. These included the top 68 DE genes between the top and bottom paths (P2 and P3) and 14 known lung cell markers ([Table S3](#)). In the CSHMM each location along a path is defined by an emission probability and so for each location we estimated the average expression value for each of these 82 genes. To assign bar-coded cells to the model we compared the expression of these genes to a densely sampled set of locations on each path (100 uniform locations). We assigned cells to the location which minimized the Euclidian distance between the bar-coded gene expression and the average expression learned for that location.

To determine the accuracy of our assignments we performed statistical tests based on randomization in which we sample a random expression profile and attempt to assign it to one of the paths in the same way we assigned the bar-coded cells. Using both t test and ranksum test on the similarity of the projected profiles to the locations they were assigned to, we concluded that bar-coded cells are significantly associated with the paths they are assigned to, further supporting our general conclusion regarding late cell fate commitment.

Isolation of SFTPC^{tdTomato}-expressing iAEC2s and Long-Term Culture of Alveolospheres

To test for long term maintenance of the lung epithelial program in iPSC-derived alveolospheres we used our published iAEC2 differentiation protocol (Jacob et al., 2017) with extensive details including serial alveolosphere passaging techniques detailed in (Jacob et al., 2019). In brief, SPC2 iPSCs were differentiated until day 16 when primordial lung progenitors were sorted based on CD47^{hi}/CD26^{neg} gating (Hawkins et al., 2017). After replating these purified progenitors in 3D Matrigel cultures in “CK+DCI” media, the resulting epithelial spheres were passaged without further sorting on day 37 and CHIR was briefly withdrawn from days 40-44 to achieve iAEC2 maturation (Jacob et al., 2017). Then CHIR was added back for the duration of the experiment. On day 51 SFTPC^{tdTomato+} cells were sorted and replated as alveolospheres with subsequent passaging *without further cell sorting* performed on days 65, 82, 101, and 115. scRNA-seq of all calcein blue-stained live cells was performed on day 115 using the 10X Chromium system with v2 chemistry as previously published (McCauley et al., 2018). Library preparation, sequencing, alignment and analyses were performed as previously published and tSNE plots with Louvain clustering and identity gene overlays prepared using our previously published pipeline (McCauley et al., 2018). Datasets are available for download from GEO (GSE137799).

Determining Fate Retention in Additional iPSC lines

For independent validation of stable SFTPC^{tdTomato+} outgrowth by scRNA-seq using iPSCs from a variety of genetic backgrounds, two additional iPSC lines, “SPC2” and “ABCA35” (clones SPC2-ST-B2 and ABCA3_W308R ST13CR17Corr18), were obtained from the Boston University CREM’s iPSC Core Facility (Boston, MA). These lines were generated by reprogramming patient-derived fibroblasts (SPC2-18 and ABCA35 from Washington University; generous gift of Drs. F. Sessions Cole, Aaron Hamvas, and Jennifer Wambach, St. Louis, MO). The Institutional Review Board of Washington University, St. Louis, MO, approved procurement of these fibroblasts with documented informed consent. SPC2-18 cells were reprogrammed using the excisable, floxed lentiviral STEMCCA vector, with successful STEMCCA excision confirmed prior to directed differentiation as previously published (Somers et al., 2010). ABCA35 cells were reprogrammed with the Sendai reprogramming system (CytoTune, ThermoFisher, Grand Island, NY). SPC2 cells originally carried a SFTPC^{C173T} heterozygous mutation and ABCA35 cells originally carried ABCA3^{W308R} homozygous mutations. After reprogramming, both lines underwent CRISPR gene editing to correct these mutations to generate control iPSC lines (K. Alysandratos et al. and Y. Sun et al. manuscripts in preparation). For tracking distal lung differentiation efficiency each line was engineered to carry a tdTomato reporter targeted to the endogenous SFTPC locus (SFTPC^{tdTomato} or “ST”) using previously published methods (Jacob et al., 2017).

QUANTIFICATION AND STATISTICAL ANALYSIS

Reverse Transcriptase Quantitative PCR

RT-qPCR was performed as previously described (Hawkins et al., 2017). Briefly, RNA was isolated according to manufacturer’s instructions using the QIAGEN miRNeasy mini kit (QIAGEN). cDNA was generated by reverse transcription of up to 150ng RNA from each sample using the Applied Biosystems High-Capacity cDNA Reverse Transcription Kit. For qPCR, technical triplicates of each of at least 3 biological replicates were run for 40 cycles as either 20 uL reactions (for use in Applied Biosystems StepOne 96-well System) or 12 uL reactions (for use in Applied Biosystems QuantStudio7 384-well System). All primers were TaqMan probes from Applied Biosystems (see all in Key Resources Table). Relative gene expression was calculated based on the average cycle (Ct) value of the technical triplicates, normalized to 18S control, and reported as fold change (2^(-DDCT)), with a fold change of 1 being assigned to untreated cells depending on the experimental conditions. Samples with undetectable expression after 40 cycles were assigned a Ct value of 40 to allow for fold change calculations.

Statistical Methods

Statistical methods relevant to each figure are outlined in the figure legend. In short, unless indicated otherwise in the figure legend, unpaired, two-tailed Student’s t tests were used to compare quantitative analyses comprising two groups of n = 3 or more samples, where each replicate (“n”) represents either entirely separate differentiations from the pluripotent stem cell stage or replicates differentiated simultaneously and sorted into separate wells. Further specifics about the replicates used in each experiment are available in the figure legends. In these cases, a Gaussian distribution and equal variance between samples was assumed as the experiments represent random samples of the measured variable. The p value threshold to determine significance was set at p = 0.05. Data for quantitative experiments is typically represented as the mean with error bars representing the standard deviation or standard error of the mean, depending on the experimental approach. These details are available in the figure legends.

DATA AND CODE AVAILABILITY

The data discussed in this publication have been deposited in NCBI’s Gene Expression Omnibus (Edgar et al., 2002) and are accessible through GEO Series accession numbers GSE131768, GSE137799, GSE137805 and GSE137811 and is also available as well on

the Kotton Lab's Bioinformatics Portal at <http://www.kottonlab.com>. Software for CSHMM is available at: <https://github.com/jessica1338/CSHMM-for-time-series-scrna-seq> and an interactive webtool for the CSHMM of the time series data is publicly accessible online at: <http://cosimo.junding.me>. SPRING visualizations of the time series data is available in an interactive form at: https://kleintools.hms.harvard.edu/tools/springViewer_1_6_dev.html?cgi-bin/client_datasets/nacho_springplot/allMerged .

ADDITIONAL RESOURCES

Further protocol information for reprogramming, iPSC/ESC cultures, directed differentiation and the production of lentiviral particles can be found at <http://www.bu.edu/dbin/stemcells/protocols.php>